RESEARCH ARTICLE

VOLCANICA

# Forecasting the location and timing of eruptive vents with a particle filter

Léa Zuccali*[α, β], Virginie Pinel†[β], and Yajing Yan[α]

[α] LISTIC, Université Savoie Mont Blanc, Annecy, France.
[β] Université Grenoble Alpes, Univ. Savoie Mont Blanc, CNRS, IRD, Univ. Gustave Eiffel, ISTerre, Grenoble, France.

## Abstract

Recent advances in magma transport modeling and the increasing density of real-time geophysical observations, available with good temporal resolution at many monitored volcanoes, can be used to improve volcanic hazard assessment. Here, we propose a new data assimilation strategy based on a particle filter to efficiently combine dynamic magma propagation models with geodetic data and forecast the location and timing of new eruptive vents. This strategy is verified on synthetic data in the case of a volcanic caldera under extensional stress field in two dimensions. In our synthetic experiment, we demonstrate the ability of the particle filter to predict where and when magma will reach the surface, provided that punctual measurements of surface displacement are available at intervals no longer than two percent of the total duration of the propagation phase. In addition, this assimilation strategy can help define the location of the deep storage zone before the eruption and to determine the volume and viscosity of the magma propagating towards the surface.

## Résumé

Les progrès récents dans la modélisation du transport du magma et l'augmentation des observations géophysiques, disponibles en temps réel pour la plupart des volcans, peuvent être utilisés pour améliorer l'évaluation des risques volcaniques. Nous proposons ici une nouvelle stratégie d'assimilation de données basée sur un filtre particulaire combinant efficacement des modèles dynamiques de propagation du magma avec des données géodésiques afin de prévoir la position et le moment de l'ouverture d'une nouvelle bouche éruptive. Cette stratégie est vérifiée sur des données synthétiques dans le cas d'une caldera volcanique soumise à un champ de contraintes en extension. Nous démontrons la capacité du filtre particulaire à prédire où et quand le magma atteindra la surface, à condition que des mesures ponctuelles du déplacement de la surface soient disponibles avec un intervalle de temps d'au moins deux pour cent de la durée totale de la phase de propagation. De plus, cette stratégie d'assimilation permet, avant l'éruption, de localiser la zone de stockage profonde et de déterminer le volume et la viscosité du magma se propageant vers la surface.

Keywords: Data assimilation; Eruption forecast; Magma propagation; Particle filter.

Submitted: 2025-12-12 | Accepted: 2026-09-02 | Published: 2026-09-10

Editor: R. Williams | Production: G. Seropian

## 1 Introduction

From a volcanic risk assessment perspective, it is fundamental to be able to determine as early as possible whether, where and when the magma, which has started to propagate from the storage zone, will reach the surface, particularly in the case of volcanic systems prone to off-center eruptions, which include widespread volcanic fields (e.g. the Auckland volcanic field [Le Corvec et al. 2013]), large calderas (e.g. Campi Flegrei area [Rivalta et al. 2019]) or rift zones (e.g. the East African Rift Zone [Pinel and Mériaux 2025]). In the upper crust, magma flows through dikes, i.e. planar sheets, by fracturing and deforming the surrounding rocks, thereby inducing seismicity and displacements of the Earth's surface [Rivalta et al. 2015]. The propagation phase is generally rapid, lasting from a few hours to a few days [Peltier et al. 2009; Parks et al. 2025]. The evolution of the position, shape and orientation of the dike can be tracked over time from the induced seismicity [Einarsson and Brandsdottir 1980; Duputel et al. 2019; Lengliné et al. 2021; Lomax et al. 2025] or classical inversions of surface displacements, recorded by either field instruments ensuring good temporal resolution or satellite imagery offering good spatial coverage and resolution [Battaglia and Bachèlery 2003; Smittarello et al. 2019; Beauducel et al. 2020]. However, as they are not based on dynamic models of magma transport, these inversion methods, even when used in near-real time, do not provide by themselves a true physics-based forecasting framework.

Meanwhile, dynamic numerical models can be used to calculate the magma pathway and velocity of propagation based on the physical properties of the magma and the Earth's crust, as well as initial conditions (e.g. local stress field, location of the magma reservoir, and overpressure) [Mériaux and Jaupart 1995; Pinel and Jaupart 2004; Pinel et al. 2017; Mantiloni et al. 2023; Blackstone et al. 2024]. Describing the full complexity of magma propagation in three dimensions remains difficult, as it requires the inclusion of complex concepts of fracture mechanics and fluid dynamics, but significant progress has recently been made in modelling non-planar propagation [Davis et al. 2021] and taking into account the coupling between viscous fluid flow and fracturing processes [Zia and Lecampion 2020; Furst et al. 2023]. Furthermore, Bayesian inversion of vent locations, which considers magma trajectories to be entirely controlled by the local stress field and therefore neglects the driving pressure of the magma, has been used to obtain information on the stress field of volcanic regions and its evolution over time, with an application to the Campi Flegrei in Italy [Rivalta et al. 2019]. This new approach, validated by analog experiments [Mantiloni et al. 2021] and tested in three

* zuccali.lea@gmail.com
† Virginie.Pinel@univ-smb.fr

dimensions on synthetic data [Mantiloni et al. 2024], is promising for long-term forecasting of vent locations and the production of probabilistic maps of future eruptive vents. On the other hand, integrating monitoring data into dynamic numerical models could also be beneficial for short-term forecasting [Poland and Anderson 2020].

Data assimilation is a technique that combines a dynamic model with past and present observations to predict the future state of an observed dynamic system, based on error statistics. This technique is well known for addressing issues in meteorology and oceanography [Daley 1991; Talagrand 1997; Carrassi et al. 2018]. Its use in volcanology is less common, but very encouraging. Taking advantage of direct satellite observations with high spatial and temporal resolution and dynamic ash dispersion models, recent studies have used an ensemble-based method to predict the concentration of volcanic ash in the atmosphere in real time [Osores et al. 2020; Pardini et al. 2020; Mingari et al. 2022; Weng et al. 2025]. Data assimilation also has recognized potential for predicting lava flows [Hyman et al. 2024]. Although data assimilation is straightforward in the case of the previous examples involving external flows with direct observations, it is less obvious how to use it to track magma flow at depth, where only indirect observations are available. However, the ensemble Kalman filter has already been successfully applied to predict the evolution of overpressure in magma chambers based on observations of surface displacement [Bato et al. 2017; Bato et al. 2018]. Despite the availability of dynamic models, to our knowledge, no previous study has applied data assimilation methods to predict the propagation of magma beneath the surface, as the lack of direct observations prevents the application of most conventional data assimilation methods. When the number of observations is limited, it is preferable to use a small number of parameters to define the dynamic model. In this scenario, characterized by a reduced number of parameters, the particle filter is particularly well-suited, with the added advantage, compared to the Ensemble Kalman filter, of being able to handle very effectively non-Gaussian error statistics. This is indeed essential in the case of magma propagation, where model errors are expected to be non-Gaussian.

Particle filter is one of the most advanced data assimilation methods. It relies on the Monte Carlo principle to approximate solutions for nonlinear state-space systems using Bayes' theorem. Specifically, it updates the probability density function (pdf) of the model, the prior pdf, with new observations to obtain the posterior pdf [Van Leeuwen 2009; Van Leeuwen 2010]. This method provides a robust framework for generating particles (samples) from the required distributions, without assuming specific model state distributions. A key advantage of the particle filter is its ability to handle nonlinear models and non-Gaussian error statistics. Therefore, it appears to be a suitable tool for predicting magma propagation trajectories and velocities.

In this paper, we present a proof-of-concept study exploring the potential of the particle filter for forecasting the timing and location of volcanic eruptions using surface displacement observations. Our approach relies on a two-dimensional (2D) model of magma propagation beneath a caldera in an extensional stress field. A simple parametric model predicts the magma dike position, orientation and shape over time based on the magma storage zone location, the amount of extension versus surface unloading, the crustal rigidity, the magma volume, viscosity and driving pressure. Induced surface displacements are then estimated using a dislocation model. The dynamic model and the link with geodetic observations are described in Section 2. The particle filter applied here is the Sequential Importance Resampling (SIR) or Bootstrap, based on the propagation of a set of particles (models) and a resampling step performed according to the relative weights of particles using the Stochastic Universal Sampling algorithm (or Systematic resampling). With this sampling algorithm, particles in accordance with observations are kept and the others are replaced by a new set of particles. After the resampling step, all particles—both those retained and those replaced by new ones at the current step—are propagated to the next step (see Section 3). The proposed data assimilation strategy is verified using synthetic observations of surface displacement generated from a set of selected parameters, the latter being considered as the ground truth (see Section 4 for the description of the experimental setup). The accuracy of the predicted location and timing of the eruption, as well as that of different model parameters (e.g. starting position, viscosity, etc.) are assessed against the ground truth. Analyses about the impact of the number of particles, the assimilation window, the density and distribution of observations are also performed (see Section 5). The potential of the proposed approach in line with the available geophysical data and its future evolution are finally discussed.

## 2 Magma ascent modeling

In order to predict the position and orientation of the dike (i.e. magma intrusion) at depth over time, we use a dynamic physical model that describes the propagation of magma based on a given set of physical and geometrical parameters. The geometrical parameters are the position of the magma source $(x_0, z_0)$. The local stress field is characterized by the ratio $R = \sigma_{\text{ext}}/P_l$ controlling the relative amount of extension $\sigma_{\text{ext}}$ and surface unloading $P_l$ and its actual influence on the magma path depends on the ratio $\gamma = P_m/P_l$ controlling the magma driving pressure $P_m$. The additional physical parameters are the magma viscosity $\mu$, the crust rigidity related to its Young's modulus $E$ and the volume of injected magma $V$. These seven parameters are referred to hereinafter as primary parameters and detailed in the next two sections. Following Mantiloni et al. [2021], we consider the case of magma propagating beneath a caldera in an extensional stress field in two dimensions (see Figure 1).

### 2.1 Magma trajectory

The stress field perturbation compared to the lithostatic stress induced by the caldera unloading is calculated analytically in 2D with plane strain approximation. This calculation is done by applying a uniform traction of amplitude $P_l$ over a lateral extent $2R_{\text{cal}}$ on an elastic homogeneous half-space using the solution proposed by Jaeger et al. [2007] and described in Watanabe et al. [2002]. We add a homogeneous extension to

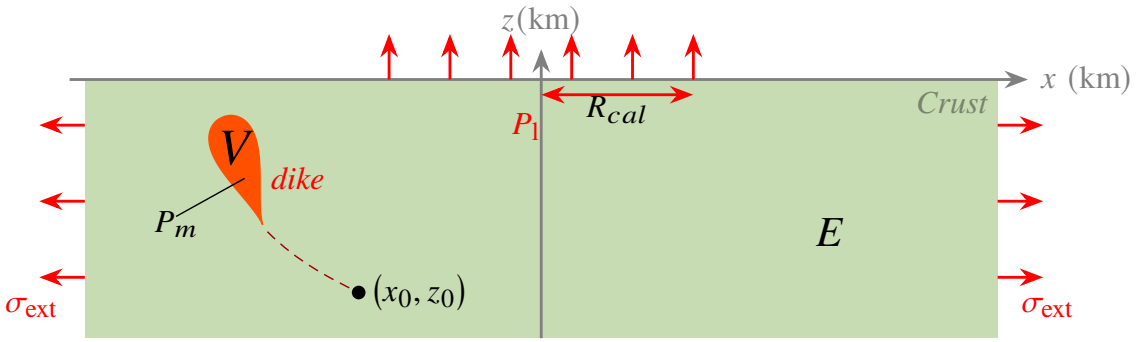



Figure 1: Illustration of the 2D case considered in this study: a caldera under extensional stress field. The caldera radius $R_{cal}$ and unloading $P_l$ are fixed. The seven model parameters are the position of the magma source $(x_0, z_0)$, the ratio $R = \sigma_{ext}/P_l$ controlling the amount of extension $\sigma_{ext}$, the ratio $\gamma = P_m/P_l$ controlling the magma driving pressure $P_m$, the magma viscosity $\mu$, the crust Young's modulus $E$ and the volume of injected magma $V$.

the horizontal component of the stress field, whose amplitude $\sigma_{ext}$ is given by the parameter $R$ defined as $R = \sigma_{ext}/P_l$. We consider the compressive stress to be positive; the expressions of the stress components are provided in Supplementary Material 1. In the first approximation, magma intrusions tend to open perpendicular to the minimum compressive stress $\sigma_3$ and thus to align with the maximum compressive stress $\sigma_1$ [Anderson 1951]. Magma path is thus often considered as tangential to $\sigma_1$ [Rivalta et al. 2019; Mantiloni et al. 2021] with a local trajectory given by the unit vector $\vec{U}_1$ associated with $\sigma_1$:

$$\vec{U}_1(x,z) = \begin{matrix} \frac{\sigma_{1,x}(x,z)}{\sigma_{1,x}^2+\sigma_{1,z}^2} \\ \frac{\sigma_{1,z}(x,z)}{\sigma_{1,x}^2+\sigma_{1,z}^2} \end{matrix} . \quad (1)$$

The amplitude and direction of the principal stress $\sigma_1$ are thus used to calculate $\vec{U}_1$ in each point. When the stress field is characterized by an horizontal extension, the maximum compressive stress $\sigma_1$ is vertical. On the contrary, beneath the caldera, providing that the unloading effect dominates over the extensional stress, the maximum compressive stress $\sigma_1$ becomes horizontal (Figure 2), as previously described [Maccaferri et al. 2014; Pinel et al. 2017]. Several studies have underlined that the magma trajectory depends not only on the local stress field but also on the magma driving pressure [Watanabe et al. 2002; Maccaferri et al. 2019], provided by the magma buoyancy and the feeding reservoir overpressure. In particular, Pinel et al. [2017] showed that the trajectory of magma lies between two extremes: when the driving pressure of the magma dominates, it rises vertically, whereas when the local stress field dominates, the magmatic intrusion follows the direction of the maximum compressive stress $\sigma_1$ and tends to be deflected laterally for magma rising beneath a caldera. The actual trajectory of the magma can be calculated using numerical models, by selecting, throughout its propagation, the path of the magma that minimises the energy released, taking into account both the effect of the local stress field and the overpressure of the magma [Maccaferri et al. 2011]. These models have been validated using analogue experiments [Maccaferri et al. 2019]. However, in this study, as we wish to calculate the trajectories of a large number of particles, we have chosen to use a simplified model, in which the local orientation of the dike is controlled by a parameter representing the balance between the magma overpressure and the amplitude of the deviatoric stress field. Indeed this is an interpolation between buoyancy/overpressure-guided and stress-guided propagation. We thus use the parameter $\gamma$, given by $\gamma = P_m/P_l$, where $P_m$ is the driving pressure of the magma. $\gamma$ is bounded between 0 and 1, it follows that the maximum magmatic overpressure allowed in our model corresponds to the magnitude of the unloading; indeed, in the case of calderas, the magmatic overpressure is expected to remain lower than the unloading. $\gamma$ is used to define the local direction of the magma path given by the effective unit vector $\vec{U}_{1,\text{eff}}$:

$$\vec{U}_{1,\text{eff}}(x,z) = \frac{(1-\gamma)\frac{\sigma_{1,x}(x,z)}{\sigma_{1,x}^2+\sigma_{1,z}^2}}{1-(1-\gamma)^2\frac{\sigma_{1,x}(x,z)^2}{\sigma_{1,x}^2+\sigma_{1,z}^2}} . \quad (2)$$

When $\gamma = 0$, the local stress field dominates and $\vec{U}_{1,\text{eff}}$ is equal to $\vec{U}_1$ (as usually considered [Rivalta et al. 2019]), whereas when $\gamma = 1$, the magma driving pressure dominates and $\vec{U}_{1,\text{eff}}$ is vertical. Since the local direction of the magma's path at each point is known, to completely define the dike's trajectory, the only remaining information needed is the initial position of the magma, given by the two additional spatial parameters, $x_0$ and $z_0$.

### 2.2 Shape and velocity of the intrusion

While the magma path is characterized by parameters $x_0$, $z_0$, $R$ and $\gamma$, other parameters are still needed to estimate the magma velocity and intrusion shape. We characterize the magmatic intrusion by its volume $V$ and viscosity $\mu$ and we use a Poisson's ratio, $\nu$, of 0.25 and a Young's modulus $E$ for the elastic crust. It should be noted that magma viscosity is considered to influence only the magma velocity, whilst the length and shape of the magma-filled crack are estimated without taking its potential effect into account.

The relationship between the volume and the length of a fluid-filled crack in three dimensions is expressed in equation

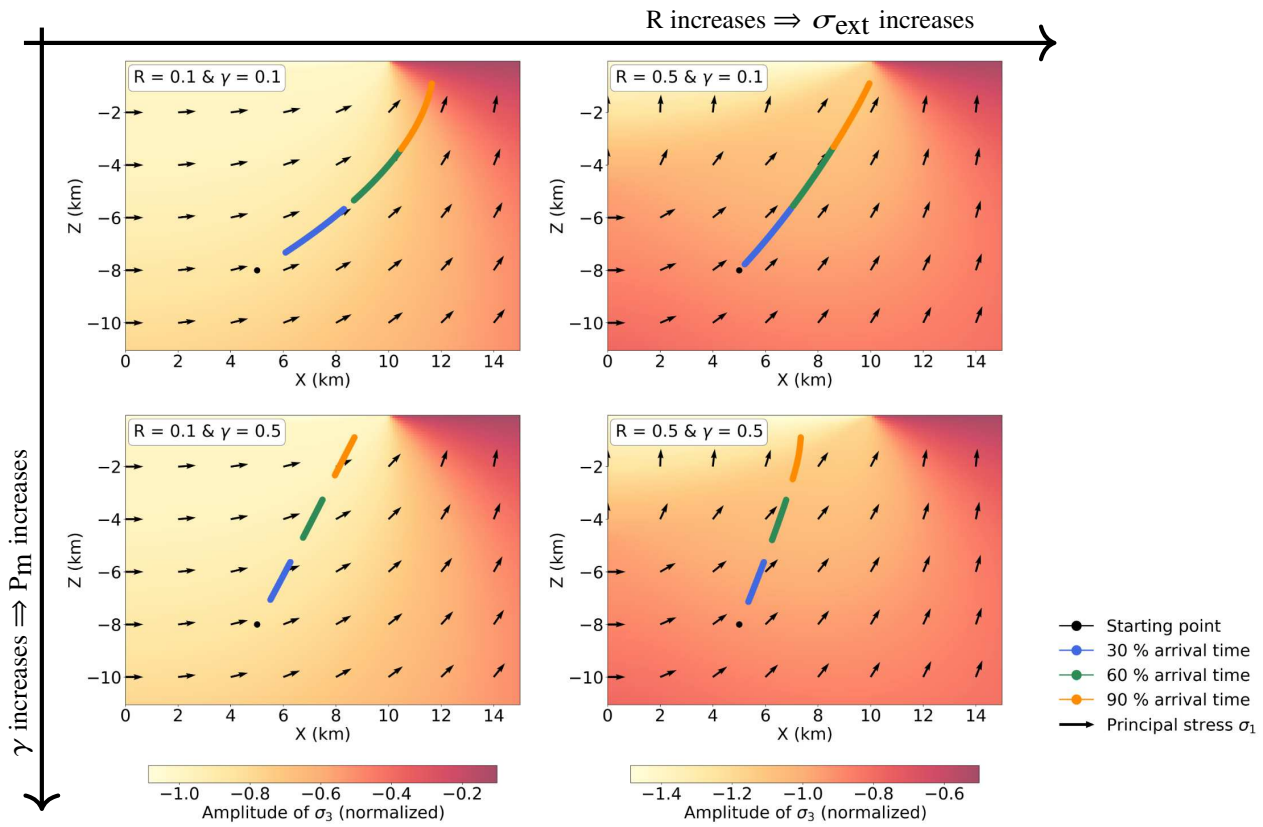



Figure 2: Simulations of magma propagation considering different values of $R$ and γ (the geometry is defined in Figure 1). The color scale is for the amplitude of the minimum deviatoric compressive stress $\sigma_3$ normalized by the unloading pressure $P_l$ (negative values are for tensile stress), black arrows are for the direction of the maximum compressive stress $\sigma_1$. The positions of the magma, at different times expressed in percentage of the time of magma arrival at the surface, are shown in blue, green and orange. The caldera radius is 10 km and $P_l$ is 15 MPa, other parameters values are set to $x_o = 5$ km, $z_o = -8$ km, $\mu = 100$ Pa·s, $V = 0.03$ km$^3$ and $E = 10^9$ Pa.

11 of Smittarello et al. [2021] for a non viscous fluid. The buoyancy effect due to the density contrast between the magma and the crust is directly linked to the magma driving pressure [Maccaferri et al. 2019]. Thus, using the definition of parameter γ, we express the magma intrusion length, $L$, as:

$$L = \left( \frac{VE}{\gamma(1-\nu^2)P_l} \right)^{1/3} \tag{3}$$

(see Supplementary Material 1 Section S2 for a full description of this equation derivation). The opening of a buoyant magmatic intrusion is not constant in depth, as it is larger in its upper part, but we consider an average opening $w$ defined as follows: $w = A/L$, where $A$ is the cross-sectional area of the fissure (along the vertical plane $x, z$) given by equation 10 of Smittarello et al. [2021] for a crack filled with a non viscous fluid. It follows that this mean opening can be expressed as:

$$w = \frac{\pi}{2}\frac{V}{L^2}. \tag{4}$$

The velocity of magma can be controlled either by viscous flow, by the fracture process, or by a combination of both, depending on the propagation regime [Detournay 2004], so that its calculation requires complex models [Zia and Lecampion 2020; Davis et al. 2023; Furst et al. 2023] and is limited by our knowledge of the crustal fracture toughness and its dependence on fracture length and velocity [Gaete et al. 2024]. In this study, in order to simplify the dynamic model, we use an empirical relationship for velocity, with the aim of capturing the first-order behaviour of magma velocity as a function of the key determining parameters. The propagation velocity of the dike increases with the volume of magma injected, as shown by experiments [Heimpel and Olson 1994] and decreases as the viscosity of the magma increases, as would be expected for any viscous flow. It should also increase with the driving pressure of the magma, characterised in our simplified model by the parameter γ. Here, for this initial proof of concept, we use the simplest formulation compatible with all these expected behaviours and define the velocity as follows:

$$v = C\frac{\gamma V}{\mu}, \tag{5}$$

where $C$ is a positive constant. This constant is chosen arbitrarily in order to obtain realistic values for the magma velocity, as described in more detail in Section 4.1.

### 2.3 Magma position and orientation over time

The magma front position at a given time $t$ is given by:

$$\vec{p_f}(t) = \vec{p_0} + \int_0^t v\,\vec{U}_{1,\text{eff}}(x(\tau), z(\tau))\,d\tau, \tag{6}$$

with $\vec{p_0} = \begin{pmatrix} x_o \\ z_o \end{pmatrix}$ the initial position of the magma.

The bottom of the magma intrusion is assumed to be at a distance $L$ from the top. If this distance has not yet been covered by the injected magma volume, the bottom of the intrusion is $\vec{p_0}$. Otherwise, we define the time $t_b$ as $t_b = t - \frac{L}{v}$ and the position of the bottom of the intrusion is:

$$\vec{p_b}(t) = \vec{p_f}(t) - \int_{t_b}^t v\,\vec{U}_{1,\text{eff}}(x(m), z(m))\,dm. \tag{7}$$

Finally, the set of trajectory points at a given time $t \geq 0$ is defined by:

$$\vec{p}(\lambda, t) = \lambda\,\vec{p_f}(t) + (1-\lambda)\,\vec{p_b}(t), \tag{8}$$

where $\lambda \in [0, 1]$, with $\lambda = 0$ corresponding to the bottom of the dike.

The magma intrusion position over time obtained by the previously described dynamic model is illustrated in Figure 2 for various values of parameters $R$ and $\gamma$. All other parameters are kept constant. As explained in Section 2.1, the parameter $R$ controls the orientation of the maximum compressive stress $\sigma_1$ (indicated by the black arrows in Figure 2), with the extension counterbalancing the effect of unloading and resulting in greater verticality of $\sigma_1$ for larger values of $R$. An increase in the parameter $\gamma$, passing from the upper panels to the lower panels, results in a more vertical magma trajectory (indicated by the colored lines) due to the larger deviation from the direction of $\sigma_1$.

We also use Equation 6, to propagate the dike until its front reaches the surface, which enables us to obtain, at each time step, the predicted time $t_e$ of the eruption, with

$$\vec{p_f}(t_e) = \begin{pmatrix} x_f(t_e) \\ z_f(t_e) = 0 \end{pmatrix} \tag{9}$$

as well as the predicted position of the eruptive vent $x_f(t_e)$.

Note that the dike can be back propagated towards its source similarly as already proposed by Mantiloni et al. [2023].

### 2.4 Link between the dynamic model and surface displacements

At each time step, we estimate the surface displacements induced by the magmatic intrusion using the solution for a rectangular dislocation embedded in an elastic half-space provided by Okada [1985]. The dike, which actually lies along a curvilinear trajectory, is for computational simplicity approximated by a straight line as shown in Figure 3A. Taking the mean between the position of the dike top $\vec{p_f} = \begin{pmatrix} x_{\text{top}} \\ z_{\text{top}} \end{pmatrix}$ and the position of the dike bottom $\vec{p_b} = \begin{pmatrix} x_{\text{bot}} \\ z_{\text{bot}} \end{pmatrix}$, we define the position of the center of the dislocation $\vec{p_c} = \begin{pmatrix} x_c \\ z_c \end{pmatrix}$. The calculation of the distance between the top and bottom points gives the length $L_o$ of the dislocation, which is slightly smaller than the intrusion length $L$ but this difference is always smaller than 10 %. The distance between the center of the dislocation and the center of the magma intrusion on the trajectory remains smaller than 50 m for 85 % of the simulations performed across all particles and all time steps in the forward simulations used to evaluate our assimilation strategy, which confirms that approximating the intrusion by a straight line does not introduce significant errors. We use the intrusion mean opening $w$ given by Equation 4 to define the opening of the dislocation. The dip, $\delta$ , is the angle with respect to the horizontal defined by:

$$\delta = \arctan\left(\frac{z_{\text{top}} - z_{\text{bot}}}{|x_{\text{top}} - x_{\text{bot}}|}\right), \tag{10}$$

and the strike $\Phi$ is taken equal to 0 for $x_{\text{top}} - x_{\text{bot}} < 0$ and $\pi$ radian for $x_{\text{top}} - x_{\text{bot}} > 0$. Since the Okada model is 3D, the lateral extent of the dike has a significant influence on the amplitude of the surface displacement it induces, yet we have no way of incorporating this parameter into our 2D proof-of-concept model. In order to overcome this limitation inherent in our 2D model we use an arbitrary value for the dislocation width (dimension along the $y$-axis), set at 1 km for all the simulated dikes. The secondary set of parameters related to the dislocation models ($x_c$,$z_c$,$L_o$,$\delta$,$\Phi$,$w$), called Okada parameters in the following, is thus defined directly from the primary parameters as illustrated in Figure 3A. Figure 3B and 3C show the vertical and horizontal displacements induced at the surface by the magmatic intrusion for different time steps. The lateral extension of the displacement decreases, while its amplitude increases as the magma approaches the surface. Consequently, the ability of geodetic observations to estimate the position and orientation of the magmatic intrusion should increase over time, whereas it is rather limited when the propagation of magma starts at depth.

## 3 Data assimilation with the particle filter

### 3.1 Particle filtering

The particle filter relies on a representation of the model Probability Density Function (pdf) by a discrete set of model states (particles) from random draws. In this study, each particle corresponds to a magmatic intrusion defined by the 7 parameters of the dynamic model. Let $m$ denote the model prediction (current position of the magmatic intrusion) and $o$ the data observations (surface displacements), the particle filter combines the model and the observations to estimate the posterior pdf of model state using the Bayes' formula:

$$p(m|o) = \frac{p(o|m)p(m)}{p(o)}, \tag{11}$$

where $p(m)$ is the *prior* probability density of $m$, $p(o|m)$ the likelihood of the observation $o$ given the model $m$, and $p(m|o)$ the *posterior* probability density function.

The optimal number of particles represents a tradeoff between the computational load and the ability to sufficiently

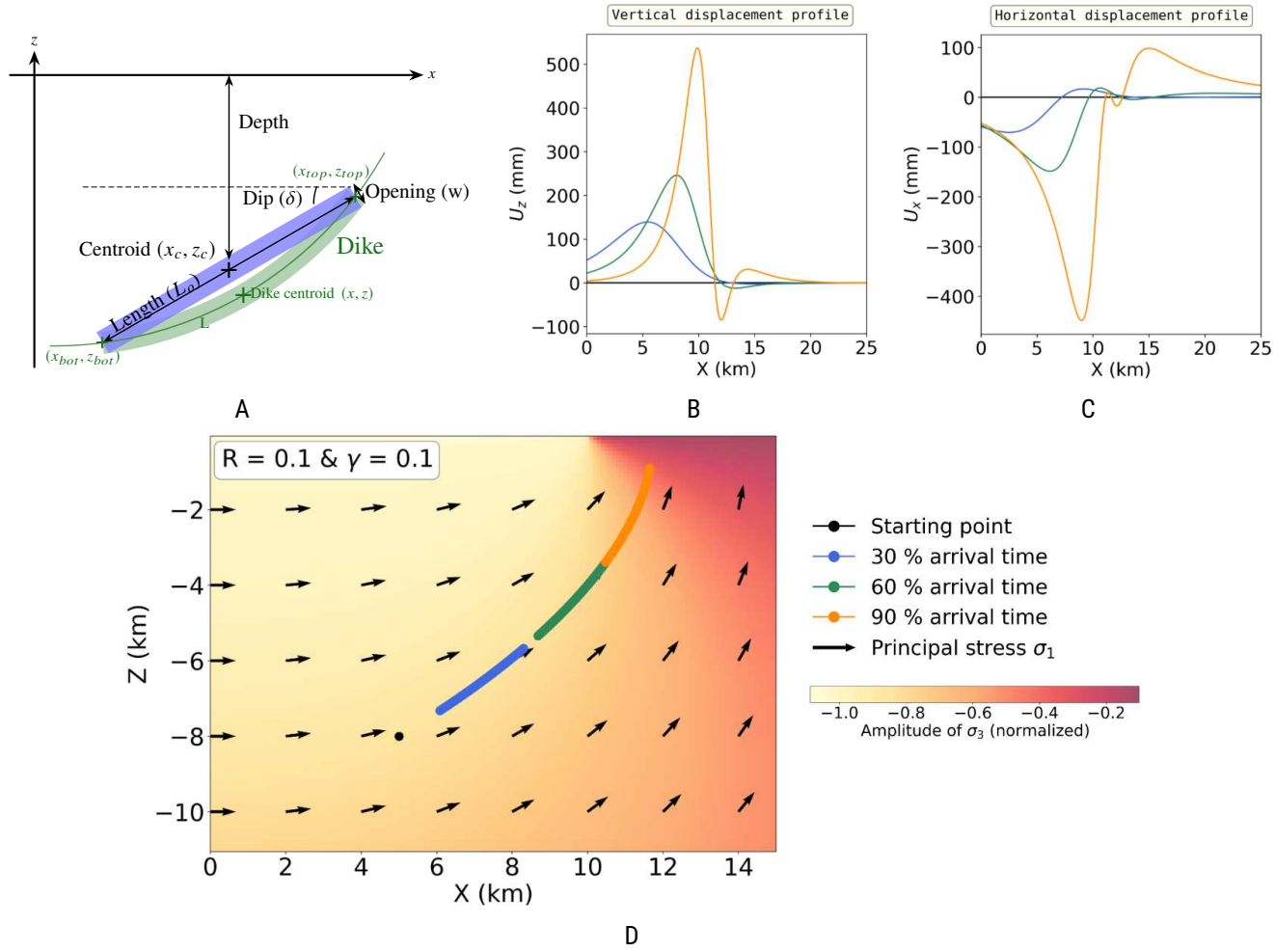



Figure 3: Dislocation model used to calculate the surface displacements induced by the magmatic intrusion. [A] Okada parameters derived from the primary parameters. [B] The vertical and [C] horizontal displacements induced at the surface (for $0 < x < 25$ km) at different time steps (colour-coded). [D] The corresponding position of the magmatic intrusion at depth (case with $R = 0.1$ and $\gamma = 0.1$ from Figure 2). Time is expressed in percentage of the time of magma arrival at the surface.

represent the model state space. Initially, all particles are assigned equal weights. Each assimilation cycle consists of two stages: forecast and analysis (Figure 4). In the forecast stage, all particles are propagated forward in time using the dynamic model's forward integration (in our case the updated position of the magmatic intrusions obtained with our dynamic model described in Section 2.3). The prior pdf of the model is represented by particles (namely forecast). In the analysis stage, the model prior pdf is updated incorporating new observations. More specifically, the likelihood for each particle is calculated by comparing the model predictions with all the available observations i.e. the vertical and horizontal displacements. In case of independent Gaussian observation errors, the likelihood is given by:

$$p(o|m) = \frac{1}{(2\pi\sigma^2)^{n/2}} \exp\left[-\frac{1}{2}\frac{||o - g(m)||^2}{\sigma^2}\right], \quad (12)$$

where σ is the standard deviation of the observation error, and $g$ the measurement operator which projects the model state on the observation space (in our case the dislocation model described in Section 2.4).

From the likelihood, a weight can be computed for each particle as:

$$w_i = \frac{p(o|m_i)}{\sum_{j=1}^{n} p(o|m_j)}, \quad (13)$$

with $n$ the total number of particles.

This weight indicates the relative closeness of each particle to the data observations, as well as its importance in the changes to the probability density. Afterward, particles are resampled based on their relative weight. Resampling results in discarding particles with low weight and duplicating those with high weight, leading, once again, to an ensemble of particles with equal weight. Several resampling algorithms are available, such as Stochastic Universal Sampling [Kitagawa 1996] (or Systematic resampling), stratified resampling, multinomial resampling or residual resampling [Li et al. 2015; Kuptametee and Aunsri 2022] and the Metropolis-Hastings algorithm [Hastings 1970]. We use an adapted version of the Stochastic Universal Sampling, as detailed in Section 3.2. After resampling, the posterior pdf of model is represented by particles (namely analysis).

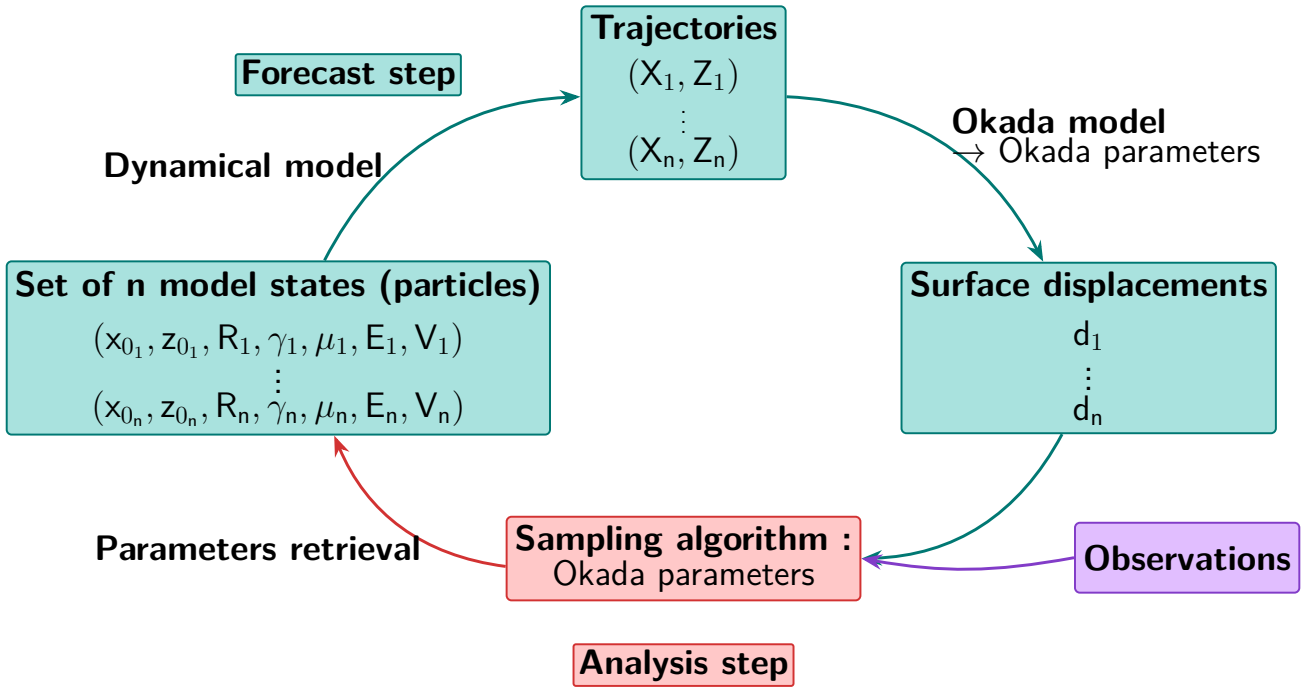



Figure 4: Illustration of an assimilation cycle with the particle filter adapted to the study. $n$ denotes the number of particles.

Figure 4 illustrates the method of the particle filter adapted to the magma propagation case. The classical strategy of the particle filter is slightly modified as the particle resampling is performed with the secondary set of parameters, i.e. the Okada parameters. It follows that an additional step is required to obtain the primary particle parameters from the Okada parameters based on physical relationships.

### 3.2 Resampling and primary parameters retrieval

For particle resampling we use the Stochastic Universal Sampling (SUS), or Systematic resampling [Kitagawa 1996; Li et al. 2015; Kuptametee and Aunsri 2022]. Detailed description of the SUS algorithm is provided in the Supplementary Material 1 Section S3. In general, the SUS provides a list of selected particles, some of which are retained several times and others resampled. Since we use a deterministic physical model to propagate the particles, the SUS algorithm, which involves the duplication of particles of high weight, would lead to severe ensemble impoverishment if applied directly. It is thus adapted (Figure 5). To avoid obtaining identical particles, we add noise to modify the Okada parameters of the resampled particles and their velocity. The preference for perturbing Okada's parameters rather than the primary parameters stems from the decision to encourage larger dispersion of the particle parameters after resampling, by combining noise with the non-uniqueness of the primary parameter inversion. In fact, preliminary tests carried out by directly altering the primary parameters did not yield satisfactory results, as the rapid and significant reduction in the dispersion of the particle parameters prevents convergence towards their true values (see Supplementary Material 1 Section S5 and Figure S5). It should be noted that this decision to perturb the Okada parameters complicates the relationship between the observations and the primary parameters and influences the posterior distribution obtained from the particle analysis. In this sense, this approach can be regarded as a heuristic rejuvenation scheme rather than a standard bootstrap particle filter.

The final step is to retrieve the primary model parameters from Okada parameters (see panel 5 of Figure 5). These parameters are retrieved by first estimating the parameters $R$ and $\gamma$ consistent with the position and dip of the intrusion. We calculate the orientation of the effective unit vector $\vec{U}_{1,\text{eff}}$ at each grid position for 399 possible combinations of the parameters $R$ and $\gamma$ ($R$ ranging from 0 to 1, with a step size of 0.05, and $\gamma$ ranging from 0.05 to 0.95 with a step size of 0.05). For each resampled particle, we calculate the probability of all combinations of parameters $R$ and $\gamma$ given the position and dip of the intrusion, and we select one combination from the 10 % most probable combinations (see Supplementary Material 1 Section S4 for a detailed description). We investigated the impact of the number of combinations retained in the selection process by varying the percentage of the most probable combinations considered from 1 % to 30 % and verified that this factor has no significant effect on our results (see Supplementary Material 1 Figure S4). Once the trajectory of the magma particle is defined by $R$ and $\gamma$, we back propagate our dynamic model, using the particle velocity slightly modified with noise, to obtain $x_0$ and $z_0$, the initial particle position. Parameters $\mu, E, V$ are then calculated, from the velocity, the length $L$ approximated to $L_o$ and the opening $w$, using Equations 3, 4 and 5. It is important to emphasize that this determination of the primary parameters is not unique, as various combinations of the parameters $R$ and $\gamma$ are compatible with the orientation of the dike (see Supplementary Material 1 Figure

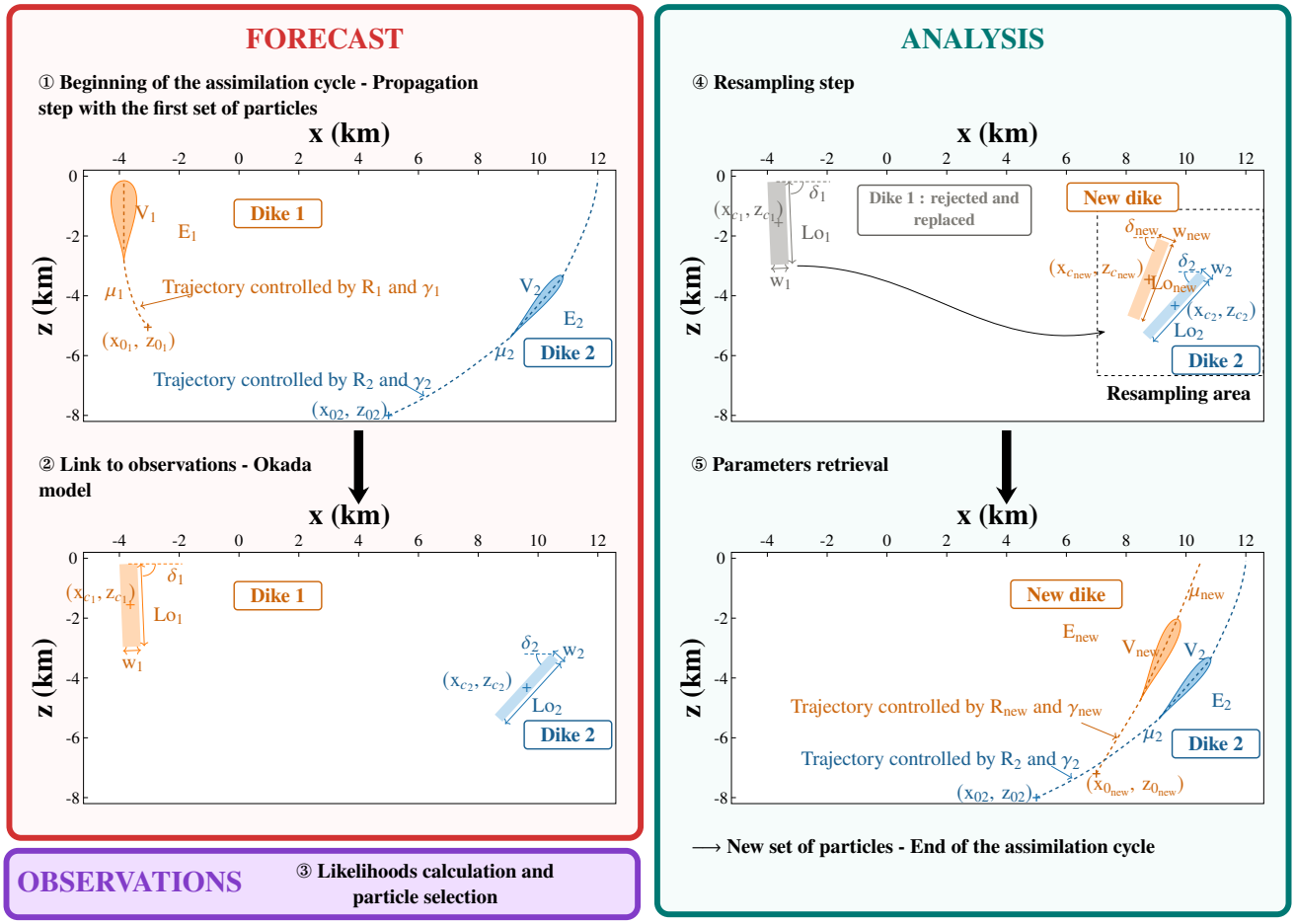



Figure 5: Particles resampling illustrated with a set of 2 particles. 1) Dike 1 (orange) and Dike 2 (blue) are both generated by a set of primary model parameters. 2) The dislocation model provides secondary parameters—the Okada parameters, directly associated to a surface displacement field. 3) Surface displacements are compared to observations. Dike 1 is rejected, while Dike 2 accepted. 4) A resampling area is created around the accepted dike. A new set of Okada parameters is created in this area by adding noise to Okada parameters of Dike 2. 5) New primary models parameters are retrieved from the new Okada parameters. A new particle with model parameters is created.

S3). However, although this step may temporarily affect the range of the parameter distribution by artificially increasing it, the tests carried out indicate that it does not appear to have a significant impact on the evolution of the mean value of the parameters.

## 4 Experimental setup used for validation in a synthetic case

### 4.1 Primary dynamic model parameters

We set the caldera radius to 10 km and the unloading due to the caldera formation, $P_l$, to 15 MPa, which corresponds to an excavation depth of approximately 500 m. The model grid extends from -30 km to 30 km along the $x$-axis (horizontal direction) and from -10 km to -100 m along the $z$-axis (vertical direction) with a spatial step of 100 m (a finer step of 10 m was also tested, which increased the computation time eightfold; the spatial resolution of the grid does not appear to have a significant impact on the results, as shown in Supplementary Material 1 Section S6 and Figure S6). The upper boundary of the grid was set at a distance of one grid step below the surface in order to ensure that the surface displacement could be calculated using the Okada solution. The position of the magma intrusion is calculated every 60 s, which corresponds to the dynamic model forward integration time step.

Table 1: Distribution of primary model parameters for particle generation and values used to generate synthetic truth. $\mathcal{U}$ denotes uniform distribution.

| Parameter | Distribution | True particle | Unit |
|---|---|---|---|
| $x_0$ | $\mathcal{U}(-15000, 15000)$ | 2000 | m |
| $z_0$ | $\mathcal{U}(-10000, -1000)$ | -8000 | m |
| $R$ | $\mathcal{U}(0, 0.6)$ | 0.5 | - |
| $\gamma$ | $\mathcal{U}(0.2, 0.8)$ | 0.5 | - |
| $\mu$ | $\mathcal{U}(100, 1000)$ | 100 | Pa.s |
| $E$ | $\mathcal{U}(10^9, 10^{10})$ | $5 \times 10^9$ | Pa |
| $V$ | $\mathcal{U}(5 \times 10^6, 5 \times 10^8)$ | $10^8$ | $m^3$ |

Table 2: Characteristics of the noise added to the Okada parameters and velocity of an accepted particle.

| Parameter | Value | Distribution | Unit |
|---|---|---|---|
| $x_{c,\text{new}}$ | $x_{c,\text{new}} = x_{c,ac} + \epsilon_x$ | $\epsilon_x \sim \mathcal{U}(-200, 200)$ | m |
| $z_{c,\text{new}}$ | $z_{c,\text{new}} = z_{c,ac} + \epsilon_z$ | $\epsilon_z \sim \mathcal{U}(-200, 200)$ | m |
| $\delta_{\text{new}}$ | $\delta_{\text{new}} = \delta_{ac} + \epsilon_\delta$ | $\epsilon_\delta \sim \mathcal{U}(-0.25, 0.25)$ | radian |
| $L_{o-\text{new}}$ | $0.5L_{o-ac} < L_{o-\text{new}} < 2L_{o-ac}$ | | m |
| $w_{\text{new}}$ | $0.5w_{ac} < w_{\text{new}} < 2w_{ac}$ | | m |
| $v_{\text{new}}$ | $v_{\text{new}} = v_{ac} + \epsilon_v$ | $\epsilon_v \sim \mathcal{U}(-0.1, 0.1)$ | m/s |

The distributions of the primary model parameters used to generate the initial random particles are described in Table 1. To ensure generality, in our proof-of-concept study, uniform distributions with a realistic range of parameters for basaltic magmatic intrusions are taken into account. The constant $C$ in Equation 5 is set to $5\times10^{-7}$ Pa·m$^{-2}$, which, with the chosen parameter distribution, ensures that particle velocities vary between $10^{-3}$ and 1 m/s, with the most probable values around 0.1 m/s. We choose one set of parameters given in Table 1 to define the synthetic truth, propagate the corresponding magmatic intrusion using the dynamic model described in Section 2.3 and produce the resulting observations as described in Section 2.4. This synthetic dike reaches the surface at the position $x = 4.15$ km and at time $t = 33234$ s such that the magma propagation duration is around 9 hours and 14 minutes, corresponding to a velocity of 0.25 m/s.

Noise following a normal distribution $N(0, 0.01)$ for the vertical displacement and $N(0, 0.001)$ for the horizontal displacement is added to the truth to generate synthetic observations. We then use these observations during the forecast step to update the particles population. If, for a given particle, the crack front reaches this upper limit before it does so for the particle chosen as the synthetic truth, the given particle is resampled as described in the Section 4.3.

### 4.2 Particle filter setting

The number of particles $n$ takes values between 50 and 300. The influence of the number of particles on the prediction accuracy will be discussed in Section 5.2. From the initial condition, a starting position $(x_o, z_o)$ at time $t = 0$, the dikes corresponding to the different particles propagate according to the dynamic model during an initial phase of 3600 s until the 60$^{\text{th}}$ time step. This initial propagation phase ensures that the particles have already propagated along their trajectories before the induced surface displacement is analyzed; this has no impact, as the ability of the surface displacement to effectively track the magma at depth is limited in the case of deep dikes. Assimilation is then performed at a given frequency controlled by the assimilation windows $\Delta w$ set between 1 % and 5 % of the total magma propagation time of the synthetic truth considered. The influence of the assimilation window will be discussed in Section 5.3. The assimilation starts at time $t = 11$ % of the total magma propagation duration after a period of free propagation. Observations used for assimilation are vertical and horizontal surface displacements distributed at $z = 0$ along the $x$-axis from -30 km to 30 km. Observations uncertainties are included by setting their standard deviation to 1 mm and 1 cm, for horizontal and vertical displacements respectively to take account of the larger uncertainty in the vertical component of the GNSS data. The number of observations used for the assimilation strongly influences the ability of the particle filter to accurately predict the magma position over time. In Section 5.4 we will discuss how the density and spatial distribution of the observations affect the results of the particle filter.

### 4.3 Adaptation of the SUS algorithm and primary parameter retrieval

By applying the SUS algorithm, some particles are retained and their parameters remain unchanged, while others are resampled by adding noise to the Okada parameters of the accepted particles.

The new Okada parameters $x_{c,\text{new}}$, $z_{c,\text{new}}$, $\delta_{\text{new}}$, $L_{o-\text{new}}$, $w_{\text{new}}$ of resampled particles are obtained by adding random noise to accepted displacement parameters $x_{c,ac}$, $z_c$, $\delta_{ac}$, $L_{o-ac}$, $w_{ac}$ as described in Table 2. For a given resampled particle, the noise added to the accepted parameter is a random value sampled from a centered uniform distribution, with realistic ranges, except for the crack length and opening, for which the accepted value is multiplied by a factor between 0.5 and 2 to ensure that the variability is proportional to the accepted value.

Primary parameters retrieval is performed as described in Section 3.2. A new velocity $v_{\text{new}}$ is determined based on the corresponding velocity of the accepted particle $v_{ac}$ as described in Table 2.

Note also that besides the particles with low weight, particles that arrive at the surface before the synthetic truth are also resampled in order to keep the same number of particles along the assimilation cycles as explained earlier. Another strategy would have been to remove the particle as soon as it reached the surface, whilst retaining its parameters, its arrival time and the location of its exit point within the distribution, in order to avoid any bias in the distribution; however, this would have led to a problematic reduction in the effective number of particles over time.

## 5 Results

We present the results of the proposed data assimilation strategy with a particle filter in different experiments in order to evaluate its potential and accuracy for predicting the location and timing of eruptive vents. In each case, the evolution over time of the predicted location of the eruptive vent (i.e. where

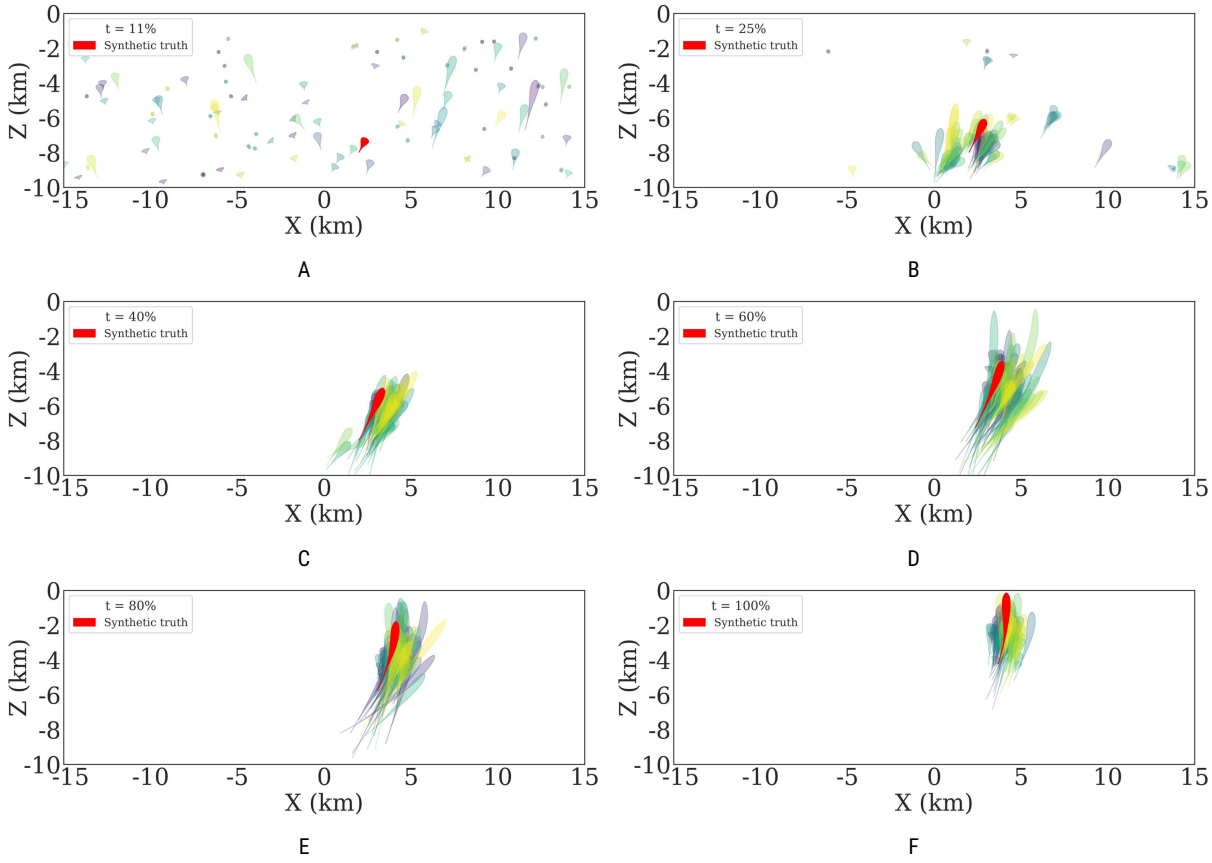



Figure 6: Evolution of the particle filter in the reference case ($n = 100$, $\Delta w = 1\,\%$, $N_o = 600$). Time is expressed in percentage of the total arrival time at the surface for the synthetic dike (truth), the synthetic dike being represented in red. Note that the represented thickness is not proportional to the actual dike opening. Particles position and length [A] just before starting the assimilation at the end of the free propagation phase at $t = 11\,\%$, [B] at $t = 25\,\%$, [C] at $t = 40\,\%$, [D] at $t = 60\,\%$, [E] at $t = 80\,\%$ and [F] at $t = 100\,\%$ when the synthetic dike reaches the surface.

magma reaches the surface) and that of the predicted arrival time of magma at the surface, $t_e$, as well as the evolution of certain primary model parameters are presented. These values are compared to the truth given by the synthetic dike. Time is always expressed as a percentage of the total magma propagation time of the synthetic truth, with $t = 0$ when magma propagation starts and $t = 100\,\%$ when the magma reaches the surface for the synthetic dike. However, it should be noted that for all figures presenting the assimilation results, the particle distributions are presented from the first assimilation step at time $t = 11\,\%$ to the last assimilation step when the truth particle arrives at the surface at $t = 100\,\%$. In addition, in some cases, the evolution over time of the normalised mean absolute error (NMAE, see the expression in Supplementary Material 1 Section S8) for the seven primary model parameters is presented in the Supplementary Material 1 Section S8. We first present a general case for verification of the proposed assimilation strategy. We then describe the effects of the number of particles $n$, the assimilation window $\Delta w$, and the density and spatial distribution of the observations.

### 5.1 General case : benefits of the method

We here consider a reference case, with a total of $n = 100$ particles, short assimilation cycles of 1 % of the total magma propagation duration, and $N_o = 600$ observed points, regularly distributed at the surface from -30 km to 30 km along the $x$-axis.

The evolution of the particles (dikes), including their position and length over time, is illustrated in Figure 6. While in the initial stage of propagation, the dikes are distributed throughout the domain (Figure 6A), they quickly cluster (as soon as the time reaches 40 % of the propagation time) around the synthetic dike (see Figure 6C), showing that surface displacement measurements are effective in controlling the correct resampling of particles during the analysis stage. This is further confirmed by the evolution over time of the predicted eruption location illustrated in Figure 7A, where the spread of the eruption location distribution decreases sharply at $t = 30\,\%$, with the mean value then slowly converging towards the actual synthetic value. The evolution of the predicted arrival time of the eruption is less accurate (Figure 7B), as a large spread is still observed after several assimilation cycles. Convergence also occurs in the final stage even if the time of eruption is overestimated: the theoretical arrival time

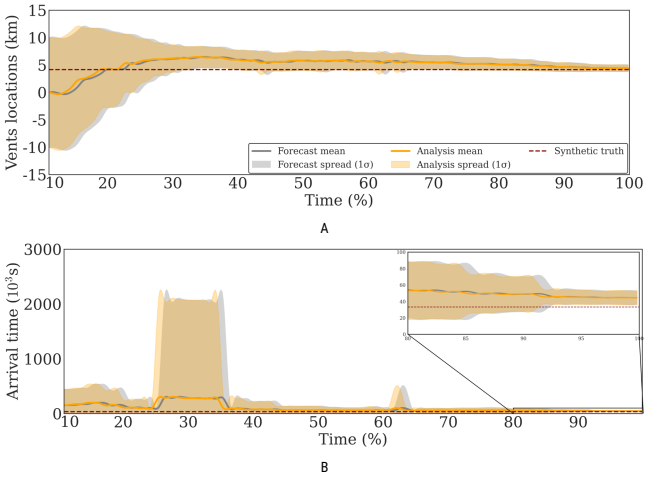



Figure 7: Predictions of the particle filter in the reference case ($n$ = 100, $\Delta w$ = 1 %, $N_o$ = 600). [A] Evolution over time of the prediction of eruptive vent location. [B] Evolution over time of the prediction of time of eruption $t_e$. The solid grey and orange lines correspond to the mean of the forecasts and the mean of the analyses, respectively. The grey and orange shaded areas correspond to the 1σ spread of the forecasts and the 1σ spread of the analyses, respectively. The theoretical value (synthetic truth) is represented by the red dashed line.

remains in the 1σ spread of the distribution until time reaches 90 % of the propagation time but the median arrival time at the final stage of assimilation is overestimated by 29 % in the reference case shown in Figure 7B, with a difference between the arrival time of the particle in the distribution closest to the synthetic particle being less than 0.1 %. This significant overestimation is probably due to the bias introduced by resampling when the magmatic intrusion approaches the surface, as all particles reaching the surface are discarded. This affects the distribution of arrival time by limiting high values in a way that is difficult to precisely quantify, as this effect becomes more pronounced as the synthetic truth approaches the surface.

The evolution over time of several model parameters is illustrated in Figure 8. Although there are some differences in the temporal evolution of their mean values and their dispersion, all estimated model parameters converge towards the synthetic truth. This occurs at approximately 30 % of the total magma propagation time for parameter $x_0$, for which a significant reduction in the spread is observed and the mean value converges towards the synthetic truth. The evolution of the dispersion is less favourable for the other parameters: no decrease in the spread for the parameter $R$ is observed, whilst a slight decrease is observed following several transient increases in the case of viscosity and volume, but the mean value converges towards the true value even when the true value lies at the limit of the initial particle distribution, i.e. outside of the 1σ spread, as in the cases of parameter $R$, magma volume or viscosity. The results for the reference case are therefore satisfactory, which provides encouraging proof-of-concept support for the proposed data assimilation strategy.

### 5.2 Influence of the particle number

In order to analyse the influence of the number of particles $n$ on the efficiency of the particle filter, we perform four different simulations with $n$ = 50, $n$ = 80, n=100, and n=300 particles, maintaining a short assimilation window with assimilation cycles representing 1 % of the total magma propagation time and integrating $N_o$ = 600 observations, evenly spaced at the surface from -30 km to 30 km on the $x$-axis.

The predictions over time of the location, timing of the eruption and parameter μ are shown in Figure 9. Additional parameters evolutions are shown in Supplementary Material 1 SectionS7, Figure S7). With $n$ = 50 particles, the convergence towards the synthetic truth seems less reliable based on this experiment, whereas using more than 80 particles allows the particle filter to achieve satisfactory efficiency with comparable results. Once again, the dispersion of the arrival time prediction does not systematically decrease with time; it is characterised by periods of high values occurring at different time steps depending on the number of particles, and similar behaviour is observed for magma viscosity (Figure 9C). These dispersion fluctuations occur mainly due to the particle resampling where random noise is added to the secondary parameters and a backpropagation step is performed to get the primary parameters. The radar diagrams in Supplementary Material 1 Figure S10 show the evolution of model parameter accuracy over time for different numbers of particles. Since the NMAE is calculated at a given time step, any temporary increase in the dispersion of a parameter's distribution leads to a bad value (close to 1) of the NMAE, as for viscosity at time t = 75 % when n = 300. It appears that some parameters are well constrained by the particle filter, in particular the starting position, magma volume and viscosity, while others are less well estimated, such as the parameters $R$ and γ and the Young's modulus of the crust $E$.

When the number of particles is increased from 100 to 300, the computation time roughly doubles and the storage capacity required for the generated files increases accordingly. Consequently, for this synthetic low-dimensional setup, the choice of 100 particles seems to be a good compromise between limited computational cost and reasonably good accuracy.

### 5.3 Importance of temporal resolution

In order to characterise the influence of the temporal resolution, i.e. the duration of the assimilation window $\Delta w$, on the efficiency of the particle filter, we perform three different simulations with $\Delta w$ = 1 %, $\Delta w$ = 2 % and $\Delta w$ = 5 % using 100 particles and integrating $N_o$ = 600 observations, evenly spaced at the surface from -30 km to 30 km on the $x$-axis.

The predictions over time of the location, timing of the eruption and the evolution over time of the parameter μ are shown in Figure 10. Additional parameters evolutions are shown in Supplementary Material 1 Figure S8. For the considered synthetic test, a maximum assimilation window of 2 % of the total duration of magma propagation, corresponding to at least 50 assimilation steps, is required to ensure good efficiency of the particle filter. Indeed when the assimilation cycle is longer than 5 %, the predictions do not converge to the theoretical values as shown in Figure 10, the arrival time pre-

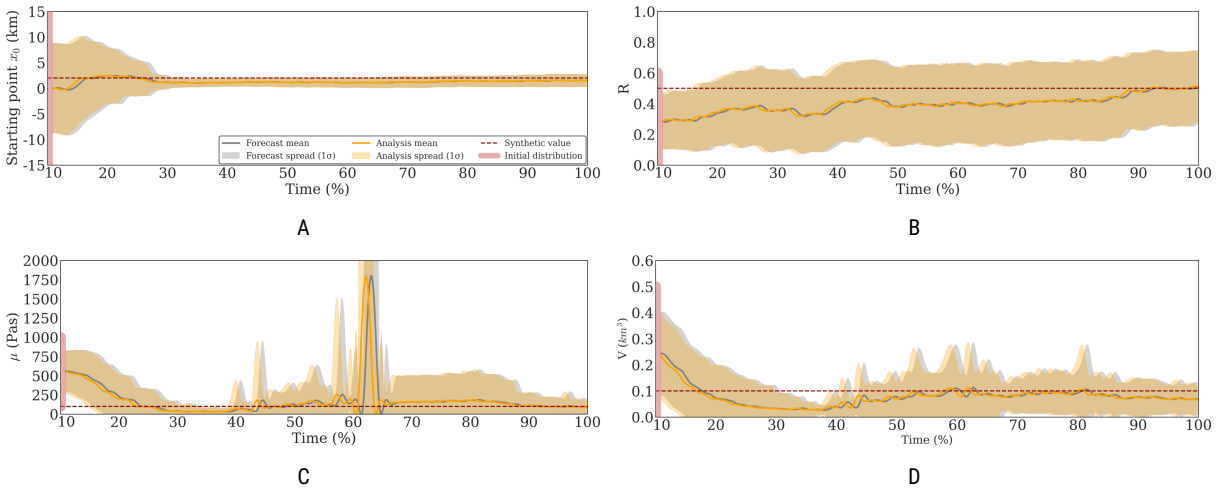



Figure 8: Parameters of the particle filter in the reference case ($n = 100$, $\Delta w = 1\,\%$, $N_o = 600$). Evolution over time of [A] starting position $x_0$, [B] parameter $R$, [C] magma viscosity μ and [D] magma volume $V$. The solid gray and orange lines correspond to the mean of the forecasts and the mean of the analyses, respectively. The gray and orange shaded areas correspond to the spread (1σ) of the forecasts and the spread of the analyses, respectively. The thick pink line on the $y$-axis corresponds to the initial range of the given parameter (see Table 1). The theoretical value (synthetic truth) is represented by the red dashed line.

diction for $\Delta w = 5\,\%$ is far from the theoretical, whereas those for $\Delta w = 1\,\%$ and $\Delta w = 2\,\%$ are rather accurate. The same observation is obtained regarding the estimations of the viscosity shown in Figure 10C. We can thus conclude that observations need to be available at a high temporal resolution for a successful application of the particle filter for eruptive vents prediction. In terms of feasibility in real conditions, this suggests that only continuously recorded geodetic data as GNSS data would likely be most suitable for this data assimilation strategy.

The radar diagrams in Supplementary Material 1 Figure S11 confirm that the starting position, magma volume and viscosity are fairly well estimated while the parameters $R$, γ and the Young's modulus of the crust $E$ are less well constrained.

### 5.4 Influence of spatial resolution and distribution

In this section, we focus on the spatial density and distribution of observations in order to determine the number of measurements required to obtain acceptable results. We consider two scenarios: in the first scenario, different simulations are performed with a given number of regularly spaced observation points $N_o$, while in the second scenario, the observations are randomly spaced on the surface. For each simulation, we take $n = 100$ particles and $\Delta w = 2\,\%$.

#### 5.4.1 *Case of regularly spaced observations*

We run 3 simulations with $N_o = 30$, $N_o = 15$ and $N_o = 5$. Observations are regularly spaced along the $x$-axis from -30 km to 30 km.

Predictions of vents location, arrival time over time and the evolution over time of the parameter μ are presented in Figure 11. Additional parameters evolutions are shown in Supplementary Material 1 Section S7, Figure S9. Predictions remain satisfactory even when only a small number of observations are integrated. For 30 or 15 observations, the reduction of the spread and the convergence of the mean value towards the synthetic truth remain similar to the case with 600 observations for the vent location and the arrival time. However, the spread remains larger and less stable than that observed for 600 observations in the case of the magma viscosity estimate. The spreads of the arrival location and starting point estimations are rapidly reduced in a significant way whereas it does not evolve a lot with time for parameters $R$ and the magma volume (see Supplementary Material 1 Figure S9). Large variations in the spread of the distribution is observed for the arrival time and viscosity estimations with only 5 observations and the mean value is significantly further from the synthetic truth.

The radar diagrams in Supplementary Material 1 Figure S12 confirm that the starting position, magma volume and viscosity are fairly well estimated while the parameters $R$, γ and the Young's modulus of the crust $E$ are less well constrained and that, for this synthetic case, at least 15 observations are needed to ensure good accuracy of the primary parameters estimation.

#### 5.4.2 *Case of randomly spaced observations*

We performed two different simulations with observations randomly distributed in space at the surface using $N_o = 5$, $N_o = 15$ and $N_o = 30$. 100 particles are considered and $\Delta w = 2\,\%$. Predictions of vents location are shown in Figure 12. Providing that more than 15 observations are used, results are not significantly influenced by the spatial distribution of the observations and predictions are similar to the ones obtained with regularly spaced observations. However when the number of observations is reduced to 5, their spatial distribution strongly affects the results of the particle filter as evidenced by the differences in Figure 12E and Figure 12F. In the first case (simulation 1), the eruptive vent location is predicted at approximately 35 % of the total magma propagation

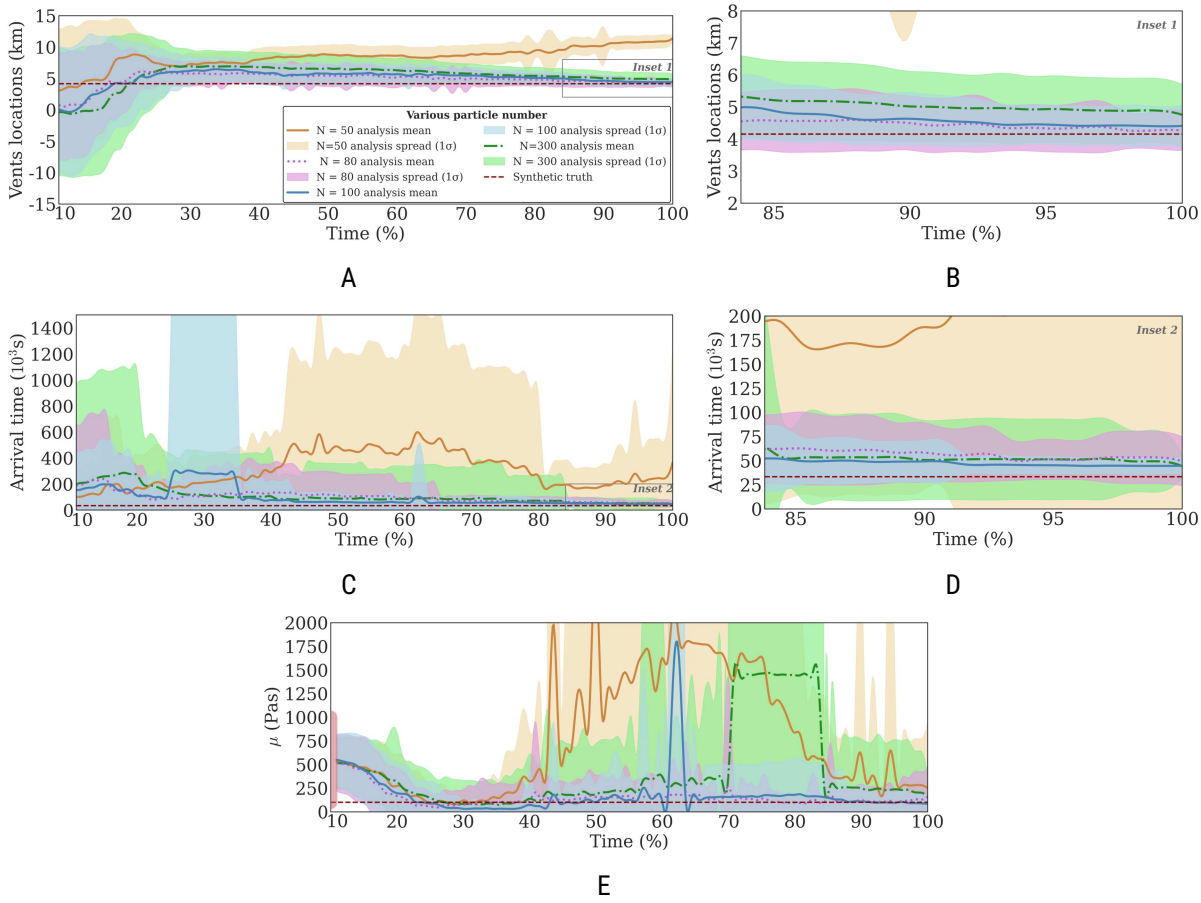



Figure 9: Predictions of the particle filter for 4 different numbers of particles: $n = 50$ in red/orange, $n = 80$ in purple, $n = 100$ in blue (reference case shown in Figure 7) and $n = 300$ in green. For each case $\Delta w = 1\,\%$ and $N_o = 600$. [A] Evolution over time of the prediction of eruptive vent location with [B] a zoom at the end of the propagation. [C] Evolution over time of the prediction of time of eruption $t_e$ with [D] a zoom at the end of the propagation. [E] Evolution over time of magma viscosity μ. The thick pink line on the $y$-axis corresponds to the initial range of the parameter (see Table 1). Lines are for the mean of the analyses and shaded areas correspond to the spread (1σ) of the analyses. The theoretical value is represented by the red dashed line.

time, while in the second case (simulation 2), it is predicted at approximately 80 % of the total magma propagation time but with a better accuracy in the end, possibly because measurement points are located farther away from the vent position but distributed on each side of this vent. In conclusion, the distribution of observations becomes critical to the success of the assimilation strategy when the available measurements are limited.

## 6 Discussion

Our initial proof-of-concept study obviously has certain limitations: the model is two-dimensional; the dynamic model used is based on simplified assumptions and parameterization, with the aim of accounting for the influence of the main physical parameters governing the magma's trajectory and velocity; we assumed uniform distributions for these parameters and the relationship between the dike and surface displacement is based on Okada's model for a rectangular dislocation, neglecting the curvature of the dike. Furthermore, our strategy has only been tested using a set of synthetic observations, considered as the 'ground truth', but generated from the dynamic model. Many further steps still need to be taken before we can achieve an operational tool capable of processing real monitoring data. For this, we propose some avenues for these steps later in the discussion. However, based on this experience, we can already draw some initial lessons. We have demonstrated the potential of the particle filter to forecast the location of an eruptive vent and the timing of an eruption using synthetic data with a simple two-dimensional propagation model. Data assimilation can be effective and also provides information on the local stress field, the position of the magma storage zone, and the volume and viscosity of the magma, provided that frequent measurements of surface displacement are available. As the magma propagation phase is generally rapid, lasting only a few hours, and assimilation windows of less than 2 % of the total propagation time are required to ensure accurate predictions, continuous geodetic measurements in the field are necessary. However, according to our simulation results, only a few measurement points, located by chance near the future eruption site, should be sufficient. A GNSS network consisting of more than five stations could therefore be sufficient to enable forecasts for real-time monitoring, even though

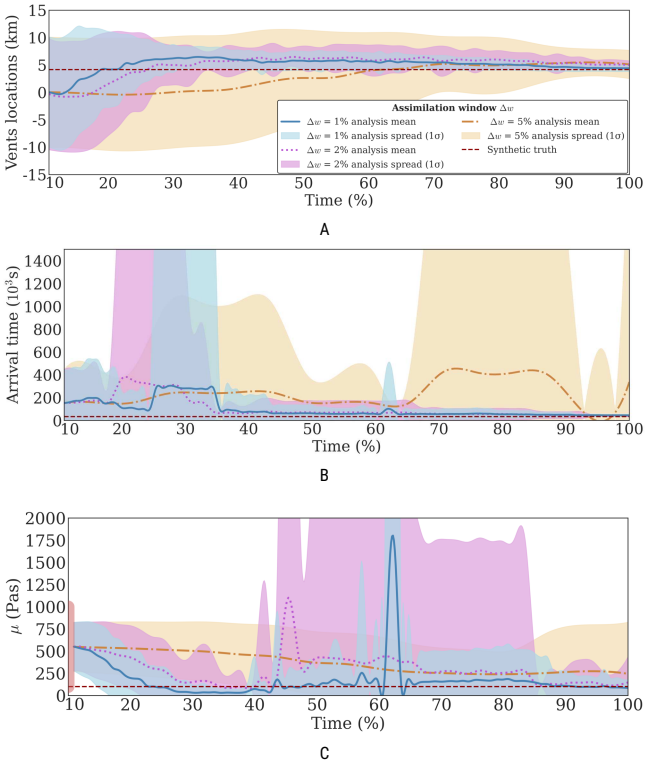



Figure 10: Predictions of the particle filter for 3 different assimilation windows: $\Delta w = 5\,\%$ in red/orange, $\Delta w = 2\,\%$ in purple and $\Delta w = 1\,\%$ in blue (reference case shown in Figure 7). For each case $n = 100$ and $N_o = 600$. [A] Evolution over time of the prediction of eruptive vent location. [B] Evolution over time of the prediction of time of eruption $t_e$. [C] Evolution over time of magma viscosity μ. The thick pink line on the $y$-axis corresponds to the initial range of the parameter (see Table 1). Lines are for the mean of the analyses and shaded areas correspond to the $1\sigma$ spread of the analyses. The theoretical value is represented by the red dashed line.

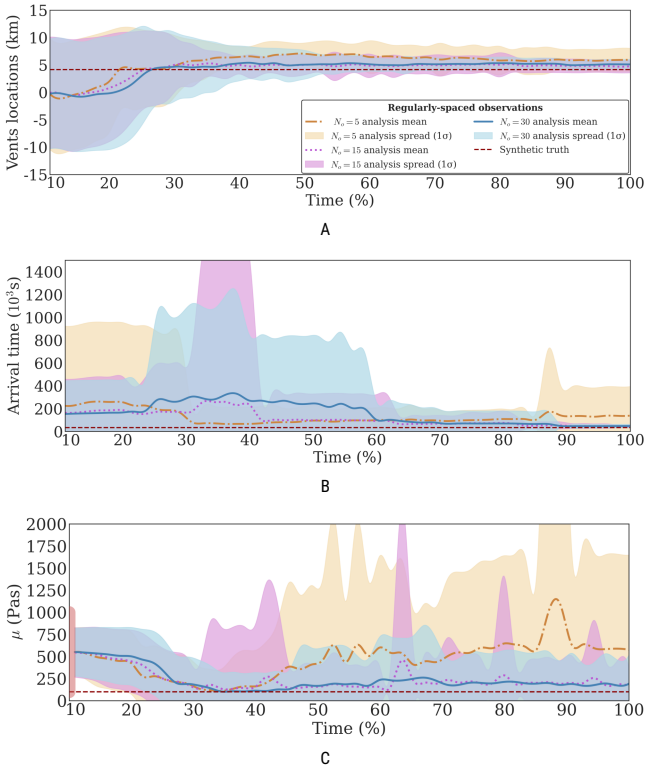



Figure 11: Predictions of the particle filter for 3 different numbers of regularly spaced observations: $N_o = 5$ in red/orange, $N_o = 15$ in purple and $N_o = 30$ in blue. For each case $n = 100$ and $\Delta w = 2\,\%$. [A] Evolution over time of the prediction of eruptive vent location. [B] Evolution over time of the prediction of time of eruption $t_e$. [C] Evolution over time of magma viscosity μ. The thick pink line on the $y$-axis corresponds to the initial range of the parameter (see Table 1). Lines are for the mean of the analyses and shaded areas correspond to the spread of the analyses. The theoretical value is represented by the red dashed line.

such networks are currently limited only to well-monitored volcanic edifices, such as Piton de la Fournaise in Réunion Island [Peltier et al. 2018], Mount Etna in Italy [Bruno et al. 2022], or Hawai'i in the United States [Montgomery-Brown et al. 2010]. On the other hand, the low temporal resolution of remote sensing data used to retrieve surface displacement, such as InSAR measurements, remains a major limitation for their use in monitoring magma propagation, as already previously highlighted [Pinel et al. 2014].

With regard to primary parameters estimation, our synthetic test shows that the location of the storage area, i.e. the starting point of magma transport, can be well defined, as well as the magma volume and viscosity. Due to the trade-off between the two parameters that control the magma's trajectory, $R$ and γ, reflecting the combined control of the magma's driving pressure and the local stress field on the magma's trajectory, it is more difficult to perfectly retrieve the local stress field. However, the actual trajectory of the magma remains well predicted. Based on the radar diagrams (see Supplementary Material 1 Section S8), it appears that our assimilation strategy fails to estimate the crust rigidity (Young's modulus). This may be less limiting in practice because rigidity can be constrained independently, for example, it can be deduced from seismic images [e.g. Currenti et al. 2007] and could be considered as known model data in the future. Similarly, parameters $R$ and γ could be better constrained if one stress parameter is estimated through additional data/information (e.g. the magnitude of tectonic stress).

The next step will be to test the proposed assimilation strategy using real observations. We could start by testing this approach using the 2D version, initially on synthetic data derived from analogue experiments, using, for instance, the experimental setup proposed by Mantiloni et al. [2021] and measuring the surface displacements due to crack propagation by photogrammetry and image correlation [Galland et al. 2016]. This 2D version could then be tried out on systems exhibiting axial symmetry—for example, on a caldera such as that of the Campi Flegrei—by taking into account, for the observations, only the distance from the centre of the caldera; or in a rift-type environment, where 2D numerical models have already been successfully applied [Maccaferri et al. 2014]. However,

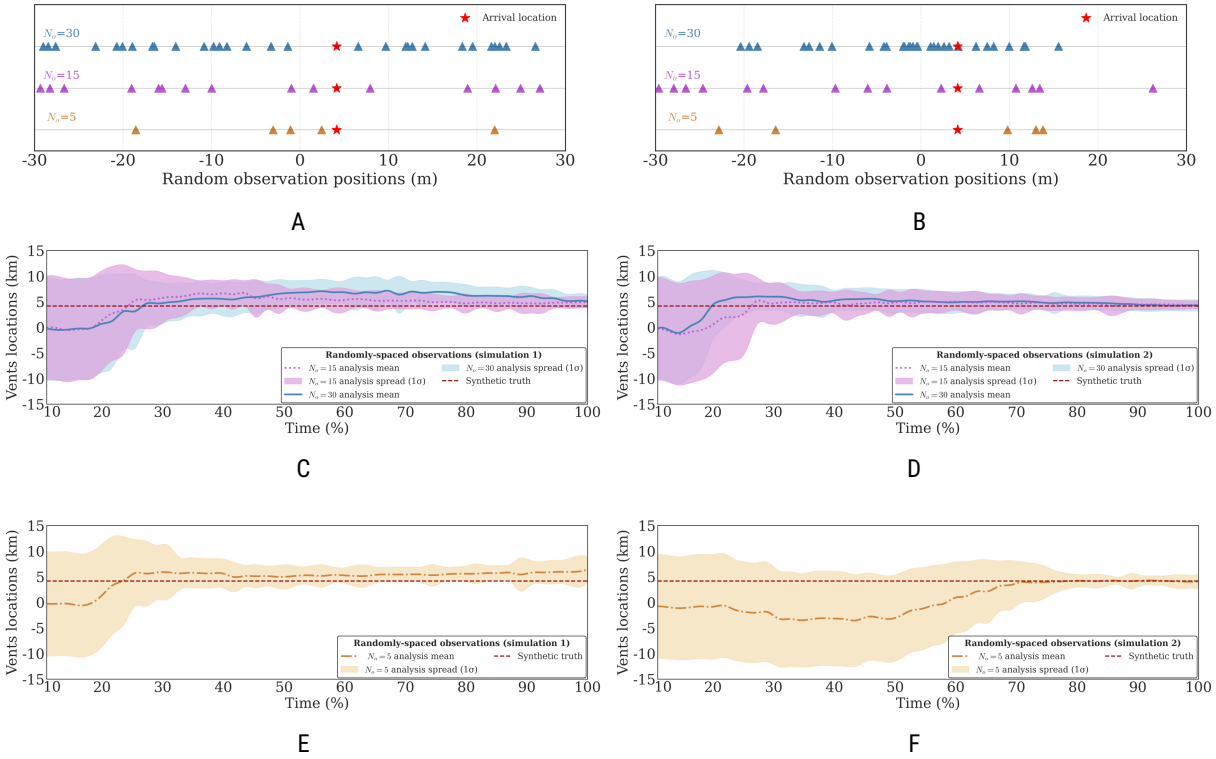



Figure 12: Predictions of the particle filter for 3 different numbers of randomly spaced observations: $N_o = 5$ % in red/orange, $N_o = 15$ in purple and $N_o = 30$ in blue. For each case $n = 100$ and $\Delta w = 2$ %, two different spatial distributions of the observations are considered corresponding respectively to simulation 1 (left panels A, C and E) and simulation 2 (right panels B, D and F). [A,B] Spatial distribution of observations along the $x$-axis with the red star showing the location of the eruptive vent for the synthetic truth. [C,D] Evolution over time of the prediction of eruptive vent location for $N_o = 15$ in purple and $N_o = 30$ in blue. [E,F] Evolution over time of the prediction of eruptive vent location for $N_o = 5$. Lines are for the mean of the analyses and shaded areas correspond to the spread of the analyses. The theoretical value is represented by the red dashed line.

in order to apply this strategy more broadly, we will need to move to 3D modelling. This will enable us to test our strategy on volcanoes that are closely monitored, where the stress field is determined by the local topography, local rift zones and detachment faults, and that experience frequent episodes of dike propagation, such as the Piton de la Fournaise [Dumont et al. 2022] , Kīlauea volcano [Montgomery-Brown et al. 2010] or Etna [Bonaccorso et al. 2002]. The transition to three-dimensional dynamic modelling will require substantial further development, but should be straightforward to achieve by following the strategy of Mantiloni et al. [2023, 2024] or using the pressure gradient as an indicator of magma trajectory [Pinel and Mériaux 2025]. Provided that the local stress can be estimated and that continuous measurements of surface displacement are available, the proposed assimilation strategy might eventually be extended to any volcanic system, even the most complex ones, involving several simultaneous magmatic pathways. Subsequently, thanks to the proposed assimilation strategy, the dynamic model can be made more complex in order to take advantage of recent advances in magma propagation modelling [Davis et al. 2021; Furst et al. 2023; Blackstone et al. 2024]. It should also be possible to include the effects of changes in magma properties during its ascent in the future. In particular, the decrease in pressure and temperature leads to magma crystallisation and/or gas exsolution, which changes the density and viscosity of the magma and affects its driving pressure (change in the $\gamma$ parameter) and velocity. The initial distribution of the model parameters could also be improved. We chose a uniform distribution for all parameters, but observations favour more appropriate distributions for certain parameters, such as the power law distribution for magma volumes [Passarelli et al. 2014].

Furthermore, we have so far only considered geodetic observations. However, magma propagation not only causes surface displacement, it also induces a seismic signal by promoting rupture or sliding on existing faults nearby, so that seismicity can be used to track the propagation of the magmatic front or the opening of the dike [e.g. Lomax et al. 2025]. It follows that the seismicity recorded during magma propagation could serve as an additional observation to constrain the assimilation. This would require incorporating a formal link between the propagating dike and the induced seismic signal, in a similar way to the link established with induced surface displacement via the Okada model. The spatial distribution of seismicity has already been linked to magmatic pressure within the dike [Segall et al. 2013; Heimisson and Segall 2020], so this observation could be added to the assimilation strategy, thereby improving predictions and parameters retrieval.

## 7 Conclusion

The potential of particle filter-based data assimilation to forecast the location of a future eruption vent and the time of magma arrival at the surface in basaltic volcanic systems where magma propagation by diking predominates has been demonstrated using synthetic data. Data assimilation has the additional advantage of providing key information on the location of magma storage zones, the volume of magma ascending to the surface, and the local stress field. This study constitutes an initial proof of concept but implementation of this three-dimensional assimilation strategy and its validation using observations recorded by volcano monitoring networks are still necessary to confirm the possibility of using this method operationally. More complex models and additional observations such as seismicity may be integrated in the future.

## Author Contributions

V.P. and Y.Y. conceptualized the study and acquired the funding. L.Z., V.P and Y.Y. developed the numerical methodology, L.Z. ran the particle filter and displayed the figures. All the authors contributed to the writing of the manuscript.

## Acknowledgements

L.Z. was funded by the ANR project AIACOPAHV. Additional financial support was provided by CNES through the TOSCA project MagmaTrack.

## Data Availability

The code for eruption forecasting based on a particle filter data using a dynamic model of magma propagation and integration of surface displacement observations is available here: https://github.com/leazuccali/ParticleFilterMagmaPropagation.

## Copyright Notice

© The Author(s) 2026. This article is distributed under the terms of the Creative Commons Attribution 4.0 International License, which permits unrestricted use, distribution, and reproduction in any medium, provided you give appropriate credit to the original author(s) and the source, provide a link to the Creative Commons license, and indicate if changes were made.

## References

Anderson, E. M. (1951). *The dynamics of faulting and dyke formation with applications to Britain: 2d ed.* London, Oliver and Boyd.

Bato, M. G., V. Pinel, and Y. Yan (2017). "Assimilation of Deformation Data for Eruption Forecasting: Potentiality Assessment Based on Synthetic Cases". *Frontiers in Earth Science* 5. DOI: 10.3389/feart.2017.00048.

Bato, M. G., V. Pinel, Y. Yan, F. Jouanne, and J. Vandemeulebrouck (2018). "Possible deep connection between volcanic systems evidenced by sequential assimilation of geodetic data". *Scientific Reports* 8(1), page 11702. DOI: 10.1038/s41598-018-29811-x.

Battaglia, J. and P. Bachèlery (2003). "Dynamic dyke propagation deduced from tilt variations preceding the March 9, 1998, eruption of the Piton de la Fournaise volcano". *Journal of Volcanology and Geothermal Research* 120, pages 289–310. DOI: 10.1016/S0377-0273(02)00410-9.

Beauducel, F., A. Peltier, A. Villié, and W. Suryanto (2020). "Mechanical Imaging of a Volcano Plumbing System From GNSS Unsupervised Modeling". *Geophysical Research Letters* 47(17). e2020GL089419, e2020GL089419. DOI: 10.1029/2020GL089419.

Blackstone, L. A., B. E. Grossman-Ponemon, E. R. Heimisson, A. J. Lew, and P. Segall (2024). "Modeling dike trajectories in a biaxial stress field with coupled magma flow, fracture, and elasticity". *Bulletin of Volcanology* 86(5). DOI: 10.1007/s00445-024-01734-8.

Bonaccorso, A., M. Aloisi, and M. Mattia (2002). "Dike emplacement forerunning the Etna July 2001 eruption modeled through continuous tilt and GPS data". *Geophysical Research Letters* 29(13), pages 2-1–2-4. DOI: 10.1029/2001GL014397.

Bruno, V., M. Aloisi, S. Gambino, M. Mattia, C. Ferlito, and M. Rossi (2022). "The Most Intense Deflation of the Last Two Decades at Mt. Etna: The 2019–2021 Evolution of Ground Deformation and Modeled Pressure Sources". *Geophysical Research Letters* 49(6). e2021GL095195, e2021GL095195. DOI: 10.1029/2021GL095195.

Carrassi, A., M. Bocquet, L. Bertino, and G. Evensen (2018). "Data assimilation in the geosciences: An overview of methods, issues, and perspectives". *WIREs Climate Change* 9(5), e535. DOI: 10.1002/wcc.535.

Currenti, G., C. Del Negro, and G. Ganci (2007). "Modelling of ground deformation and gravity fields using finite element method: an application to Etna volcano". *Geophys. J. Int.* 169, pages 775–786. DOI: 10.1111/j.1365-246X.2007.03380.x.

Daley, R. (1991). *Atmospheric Data Analysis*. Cambridge Atmospheric and Space Science Series, Cambridge University Press, 457 p.

Davis, T., M. Bagnardi, P. Lundgren, and E. Rivalta (2021). "Extreme Curvature of Shallow Magma Pathways Controlled by Competing Stresses: Insights From the 2018 Sierra Negra Eruption". *Geophysical Research Letters* 48(13), e2021GL093038. DOI: 10.1029/2021GL093038.

Davis, T., E. Rivalta, D. Smittarello, and R. F. Katz (2023). "Ascent rates of 3-D fractures driven by a finite batch of buoyant fluid". *Journal of Fluid Mechanics* 954, A12. DOI: 10.1017/jfm.2022.986.

Detournay, E. (2004). "Propagation Regimes of Fluid-Driven Fractures in Impermeable Rocks." *International Journal of Geomechanics* 4(1), pages 35–35-45. DOI: 10.1061/(ASCE)1532-3641(2004)4:1(35).

Dumont, Q., V. Cayol, J.-L. Froger, and A. Peltier (2022). "22 years of satellite imagery reveal a major destabilization structure at Piton de la Fournaise". *Nature Communications* 13(1). DOI: 10.1038/s41467-022-30109-w.

Duputel, Z., O. Lengliné, and V. Ferrazzini (2019). "Constraining Spatiotemporal Characteristics of Magma Migration at Piton De La Fournaise Volcano From Pre-eruptive Seismicity". *Geophysical Research Letters* 46(1), pages 119–127. DOI: 10.1029/2018GL080895.

Einarsson, P. and B. Brandsdottir (1980). "Seismological evidence for lateral magma intrusion during the 1978 deflation of the Krafla Volcano in NE Iceland". *Journal of Geophysics* 47, pages 160–165.

Furst, S., F. Maccaferri, and V. Pinel (2023). "Modeling the shape and velocity of magmatic intrusions, a new numerical approach". *Journal of Geophysical Research: Solid Earth*, e2022JB025697. DOI: 10.1029/2022JB025697.

Gaete, A., F. Maccaferri, S. Furst, and V. Pinel (2024). "Investigating the velocity of magmatic intrusions and its relation with rock fracture toughness: insights from laboratory experiments and numerical models". *Geophysical Journal International* 240(1), pages 638–651. DOI: 10.1093/gji/ggae396.

Galland, O., H. S. Bertelsen, F. Guldstrand, L. Girod, R. F. Johannessen, F. Bjugger, S. Burchardt, and K. Mair (2016). "Application of open-source photogrammetric software MicMac for monitoring surface deformation in laboratory models". *Journal of Geophysical Research: Solid Earth* 121(4), pages 2852–2872. DOI: 10.1002/2015JB012564.

Hastings, W. K. (1970). "Monte Carlo sampling methods using Markov chains and their applications". *Biometrika* 57(1), pages 97–109. DOI: 10.1093/biomet/57.1.97.

Heimisson, E. R. and P. Segall (2020). "Physically consistent modeling of dike induced deformation and seismicity: Application to the 2014 Bárðarbunga dike, Iceland". *Journal of Geophysical Research: Solid Earth*, e2019JB018141. DOI: 10.1029/2019JB018141.

Heimpel, M. and P. Olson (1994). "Chapter 10 Buoyancy-Driven Fracture and Magma Transport through the Lithosphere: Models and Experiments". *Magmatic Systems*. Elsevier, pages 223–240. ISBN: 9780126050707. DOI: 10.1016/s0074-6142(09)60098-x.

Hyman, D. M. R., H. R. Dietterich, E. Gallant, K. J. Lynn, M. H. Zoeller, M. R. Patrick, J. Kauahikaua, F. Trusdell, K. Hon, R. P. Denlinger, N. L. Foks, R. L. Lee, J. Falgout, and J. Gordon (2024). "Real-time lava flow forecasting during the 2022 Mauna Loa eruption response". *Bulletin of Volcanology* 87(1), page 3. DOI: 10.1007/s00445-024-01783-z.

Jaeger, J. C., N. G. W. Cook, and R. Zimmerman (2007). "Fundamentals of Rock Mechanics". 4th edition. Chichester, England: Wiley-Blackwell.

Kitagawa, G. (1996). "Monte Carlo Filter and Smoother for Non-Gaussian Nonlinear State Space Models". *Journal of Computational and Graphical Statistics* 5(1), pages 1–25. DOI: 10.1080/10618600.1996.10474692.

Kuptametee, C. and N. Aunsri (2022). "A review of resampling techniques in particle filtering framework". *Measurement* 193, page 110836. DOI: 10.1016/j.measurement.2022.110836.

Le Corvec, N., M. S. Bebbington, J. M. Lindsay, and L. E. McGee (2013). "Age, distance, and geochemical evolution within a monogenetic volcanic field: Analyzing patterns in the Auckland Volcanic Field eruption sequence". *Geochemistry, Geophysics, Geosystems* 14(9), pages 3648–3665. DOI: 10.1002/ggge.20223.

Lengliné, O., Z. Duputel, and P. Okubo (2021). "Tracking dike propagation leading to the 2018 Kīlauea eruption". *Earth and Planetary Science Letters* 553, page 116653. DOI: 10.1016/j.epsl.2020.116653.

Li, T., M. Bolic, and P. M. Djuric (2015). "Resampling Methods for Particle Filtering: Classification, implementation, and strategies". *IEEE Signal Processing Magazine* 32(3), pages 70–86. DOI: 10.1109/MSP.2014.2330626.

Lomax, A., V. Anagnostou, V. Karakostas, S. P. Hicks, and E. Papadimitriou (2025). "The 2025 Santorini unrest unveiled: Rebounding magmatic dike intrusion with triggered seismicity". *Science* 390(6775), eadz8538. DOI: 10.1126/science.adz8538.

Maccaferri, F., M. Bonafede, and E. Rivalta (2011). "A quantitative study of the mechanisms governing dike propagation, dyke arrest and sill formation". *Journal of Volcanology and Geothermal Research* 208, pages 39–50. DOI: 10.1016/j.jvolgeores.2011.09.001.

Maccaferri, F., D. Smittarello, V. Pinel, and V. Cayol (2019). "On the Propagation Path of Magma-Filled Dikes and Hydrofractures: The Competition Between External Stress, Internal Pressure, and Crack Length". *Geochemistry, Geophysics, Geosystems* 20(4), pages 2064–2081. DOI: 10.1029/2018GC007915.

Maccaferri, F., E. Rivalta, D. Keir, and V. Acocella (2014). "Off-rift volcanism in rift zones determined by crustal unloading". *Nature Geoscience* 7(4), pages 297–300. DOI: 10.1038/ngeo2110.

Mantiloni, L., T. Davis, A. B. Gaete Rojas, and E. Rivalta (2021). "Stress Inversion in a Gelatin Box: Testing Eruptive Vent Location Forecasts With Analog Models". *Geophysical Research Letters* 48(6). e2020GL090407, e2020GL090407. DOI: 10.1029/2020GL090407.

Mantiloni, L., E. Rivalta, K. R. Anderson, T. Davis, and L. Passarelli (2024). "Physics-Based Forecasts of Eruptive Vent Locations at Calderas". *Journal of Geophysical Research: Solid Earth* 129(9). e2023JB028409, e2023JB028409. DOI: 10.1029/2023JB028409.

Mantiloni, L., E. Rivalta, and T. Davis (2023). "Mechanical Modeling of Pre-Eruptive Magma Propagation Scenarios at Calderas". *Journal of Geophysical Research: Solid Earth* 128(3), e2022JB025956. DOI: 10.1029/2022JB025956.

Mériaux, C. and C. Jaupart (1995). "Simple fluid dynamic models of volcanic rift zones". *Earth and Planetary Science Letters* 136, pages 223–240. DOI: 10.1016/0012-821X(95)00170-H.

Mingari, L., A. Folch, A. T. Prata, F. Pardini, G. Macedonio, and A. Costa (2022). "Data assimilation of volcanic aerosol observations using FALL3D+PDAF". *Atmospheric Chemistry and Physics* 22(3), pages 1773–1792. DOI: 10.5194/acp-22-1773-2022.

Montgomery-Brown, E. K., D. K. Sinnett, M. Poland, P. Segall, T. Orr, H. Zebker, and A. Miklius (2010). "Geodetic evidence for en echelon dike emplacement and concurrent slow slip during the June 2007 intrusion and eruption at Kīlauea volcano, Hawai'i". *Journal of Geophysical Research: Solid Earth* 115(B7). DOI: 10.1029/2009JB006658.

Okada, Y. (1985). "Surface deformation due to shear and tensile faults in a half-space". *Bulletin of the Seismological Society of America* 75(4), pages 1135–1154. DOI: 10.1785/bssa0750041135.

Osores, S., J. Ruiz, A. Folch, and E. Collini (2020). "Volcanic ash forecast using ensemble-based data assimilation: an ensemble transform Kalman filter coupled with the FALL3D-7.2 model (ETKF–FALL3D version 1.0)". *Geoscientific Model Development* 13(1), pages 1–22. DOI: 10.5194/gmd-13-1-2020.

Pardini, F., S. Corradini, A. Costa, T. Esposti Ongaro, L. Merucci, A. Neri, D. Stelitano, and M. de'Michieli Vitturi (2020). "Ensemble-Based Data Assimilation of Volcanic Ash Clouds from Satellite Observations: Application to the 24 December 2018 Mt. Etna Explosive Eruption." *Atmosphere 2020* 11(359). DOI: 10.3390/atmos11040359.

Parks, M., V. Drouin, F. Sigmundsson, Á. R. Hjartardóttir, H. Geirsson, G. B. Pedersen, J. M. Belart, S. Barsotti, C. Lanzi, K. Vogfjörd, A. Hooper, B. Ófeigsson, S. Hreinsdóttir, E. B. Gestsson, R. H. Þrastarson, P. Einarsson, V. Tolpekin, D. Rotheram-Clarke, S. R. Gunnarsson, B. V. Óskarsson, and V. Pinel (2025). "2023–2024 inflation-deflation cycles at Svartsengi and repeated dike injections and eruptions at the Sundhnúkur crater row, Reykjanes Peninsula, Iceland". *Earth and Planetary Science Letters* 658, page 119324. DOI: 10.1016/j.epsl.2025.119324.

Passarelli, L., E. Rivalta, and A. Shuler (2014). "Dike intrusions during rifting episodes obey scaling relationships similar to earthquakes". *Scientific Reports* 4(1), page 3886. DOI: 10.1038/srep03886.

Peltier, A., N. Villeneuve, V. Ferrazzini, S. Testud, A. T. Hassen, P. Boissier, and P. Catherine (2018). "Changes in the Long-Term Geophysical Eruptive Precursors at Piton de la Fournaise: Implications for the Response Management". *Frontiers in Earth Science* 6(22). DOI: 10.3389/feart.2018.00104.

Peltier, A., P. Bachèlery, and T. Staudacher (2009). "Magma transport and storage at Piton de La Fournaise (La Réunion) between 1972 and 2007: A review of geophysical and geochemical data". *Journal of Volcanology and Geothermal Research* 184(1), pages 93–108. DOI: https://doi.org/10.1016/j.jvolgeores.2008.12.008.

Pinel, V., A. Carrara, F. Maccaferri, E. Rivalta, and F. Corbi (2017). "A two-step model for dynamical dike propagation in two-dimensions: Application to the July 2001 Etna eruption". *Journal of Geophysical Research: Solid Earth*. 2016JB013630. DOI: 10.1002/2016JB013630.

Pinel, V. and C. Jaupart (2004). "Magma storage and horizontal dyke injection beneath a volcanic edifice". *Earth and Planetary Science Letters* 221(1-4), pages 245–262. DOI: 10.1016/s0012-821x(04)00076-7.

Pinel, V., M. Poland, and A. Hooper (2014). "Volcanology: Lessons learned from Synthetic Aperture Radar imagery". *Journal of Volcanology and Geothermal Research* 289, pages 81–113. DOI: 10.1016/j.jvolgeores.2014.10.010.

Pinel, V. and C. A. Mériaux (2025). "Subsurface lateral magma propagation from Nyiragongo volcano in the Western Rift Zone of the East African Rift". *Journal of African Earth Sciences* 226, page 105569. DOI: 10.1016/j.jafrearsci.2025.105569.

Poland, M. P. and K. R. Anderson (2020). "Partly Cloudy With a Chance of Lava Flows: Forecasting Volcanic Eruptions in the Twenty-First Century". *Journal of Geophysical Research: Solid Earth* 125(1), e2018JB016974. DOI: 10.1029/2018JB016974.

Rivalta, E., F. Corbi, L. Passarelli, V. Acocella, T. Davis, and M. A. Di Vito (2019). "Stress inversions to forecast magma pathways and eruptive vent location". *Science Advances* 5(7). DOI: 10.1126/sciadv.aau9784.

Rivalta, E., B. Taisne, A. Bunger, and R. Katz (2015). "A review of mechanical models of dike propagation: Schools of thought, results and future directions". *Tectonophysics* 638, pages 1–42. DOI: 10.1016/j.tecto.2014.10.003.

Segall, P., A. L. Llenos, S.-H. Yun, A. M. Bradley, and E. M. Syracuse (2013). "Time-dependent dike propagation from joint inversion of seismicity and deformation data". *Journal of Geophysical Research: Solid Earth* 118(11), pages 5785–5804. DOI: 10.1002/2013JB010251.

Smittarello, D., V. Cayol, V. Pinel, A. Peltier, J.-L. Froger, and V. Ferrazzini (2019). "Magma Propagation at Piton de la Fournaise From Joint Inversion of InSAR and GNSS". *Journal of Geophysical Research: Solid Earth* 124(2), pages 1361–1387. DOI: 10.1029/2018JB016856.

Smittarello, D., V. Pinel, F. Maccaferri, S. Furst, E. Rivalta, and V. Cayol (2021). "Characterizing the physical properties of gelatin, a classic analog for the brittle elastic crust, insight from numerical modeling". *Tectonophysics* 812, page 228901. DOI: 10.1016/j.tecto.2021.228901.

Talagrand, O. (1997). "Assimilation of Observations, an Introduction (Special Issue Data Assimilation in Meteology and Oceanography: Theory and Practice)". *Journal of the Meteorological Society of Japan. Ser. II* 75(1B), pages 191–209. DOI: 10.2151/jmsj1965.75.1B_191.

Van Leeuwen, P. J. (2010). "Nonlinear data assimilation in geosciences: an extremely efficient particle filter". *Quarterly Journal of the Royal Meteorological Society* 136(653), pages 1991–1999. DOI: 10.1002/qj.699.

Van Leeuwen, P. J. (2009). "Particle Filtering in Geophysical Systems". *Monthly Weather Review* 137, pages 4089–4114. DOI: 10.1175/2009MWR2835.1.

Watanabe, T., T. Masuyama, K. Nagaoka, and T. Tahara (2002). "Analog experiments on magma-filled cracks: Competition between external stresses and internal pressure". *Earth, Planets and Space* 54(12), pages 1247–1261. DOI: 10.1186/bf03352453.

Weng, Z., L. Zhu, J. Li, Y. Zhang, X. Liu, W. Su, H. Sun, and X. Li (2025). "Using EnKF Data Assimilation to Improve Predictions of Volcanic Ash Dispersion". *Journal of Geophysical Research: Atmospheres* 130(8). e2024JD042215, e2024JD042215. DOI: 10.1029/2024JD042215.

Zia, H. and B. Lecampion (2020). "PyFrac: A planar 3D hydraulic fracture simulator". *Computer Physics Communications* 255, page 107368. DOI: 10.1016/j.cpc.2020.107368.